Inclusive Spin Structure Functions of the Deuteron

J.Yun and S.E.Kuhn
Old Dominion University
March 2002

Contents

Chapter 1

Introduction

Inclusive double spin asymmetries have been measured in $\vec{d}(\vec{e},e')$ using the CLAS detector and a polarized $N\vec{D}_3$ target at Jefferson Lab in 1998. The goal of these measurements is to study the spin structure of the deuteron and the neutron in the low Q^2 transition region between the real photon point, where the Gerasimov-Drell-Hearn (GDH) sum rule is expected to be satisfied, and the deep inelastic scattering limit. The analysis and the results for virtual photon asymmetries, the spin structure function $g_1^d(x, Q^2)$ and its first moment within a Q^2 range of 0.3 GeV^2 to 1.2 GeV^2 are discussed in this note. In the following, we introduce the relevant definitions and relationships and give an overview of the goals of the experiment (Chapter 2). We discuss the analysis in detail in Chapter 3 and present our results in Chapter 4.

Chapter 2

Theoretical Background

2.1 Electron-Nucleon Scattering

Electron scattering is a useful tool for investigating the structure of the nucleons. Electrons are point-like objects without any internal structure, as far as we know and the electromagnetic interactions of electrons are well understood. Electron-nucleon scattering can be expressed in first order by the one photon exchange process as shown in Fig.2.1. The kinematic parameters are defined as

$$\nu = E - E^{'} \tag{2.1}$$

$$\vec{q} = \vec{k} - \vec{k'} \tag{2.2}$$

$$Q^2 = -q^2 = (p - p^{'})^2 = 4EE^{'}\sin^2(\theta/2) \tag{2.3}$$

$$W^2 = p'^2 = M^2 + 2M\nu - Q^2 \tag{2.4}$$

$$x = Q^2/2M\nu \tag{2.5}$$

with the rest mass M of the stationary target nucleon, incoming electron beam energy E and outgoing $E^{'}$ of the scattered electron, incoming electron momentum $\vec{k}$ and the scattered electron momentum $\vec{k'}$, the electron scattering angle θ, the energy transfer ν, four-momentum transfer squared Q^2 and the final state invariant mass

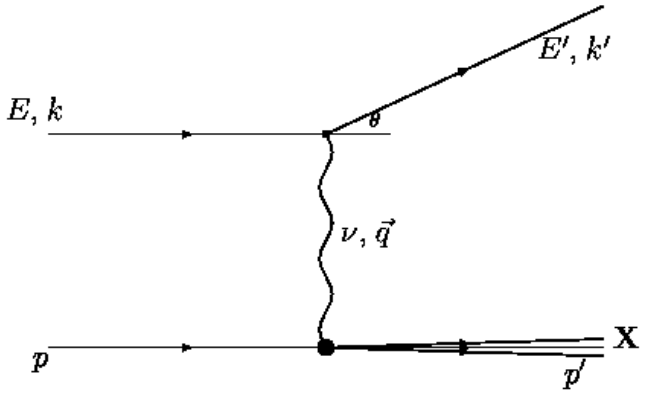

Figure 2.1: Electron-Nucleon Scattering.

squared W^2. The Bjorken scaling variable x can be interpreted as the fraction of the (longitudinal) proton momentum carried by the struck quark in the Parton Model. For a massless electron of energy E striking a stationary nucleon of mass M, the scattering cross section can be written

$$\frac{d\sigma}{d\Omega dE'} = \frac{\alpha^2}{q^4}\frac{E'}{E}L^{\mu\nu}W_{\mu\nu} \tag{2.6}$$

where $L^{\mu\nu}$ represents the lepton tensor, $W_{\mu\nu}$ is the hadronic tensor and α is the fine structure constant. The hadronic tensor can be expressed in terms of four structure functions which become a function of x only in the scaling limit:

$$F_1(x, Q^2) = MW_1(\nu, Q^2) \tag{2.7}$$

$$F_2(x, Q^2) = \nu W_2(\nu, Q^2) \tag{2.8}$$

$$g_1(x, Q^2) = M^2\nu G_1(\nu, Q^2) \tag{2.9}$$

$$g_2(x,Q^2) = M\nu^2 G_2(\nu,Q^2) \tag{2.10}$$

where F_1, F_2 are unpolarized structure functions and g_1, g_2 are polarized structure functions.

If the lepton and the target nucleon are both logitudinally polarized, the unpolarized and polarized structure functions are related to the spin averaged and spin weighted differential cross sections.

$$\frac{d^2\sigma^{\downarrow\uparrow}}{d\Omega dE'} + \frac{d^2\sigma^{\uparrow\uparrow}}{d\Omega dE'} = \frac{8\alpha^2 E'^2}{MQ^4}\left[2\sin^2\frac{\theta}{2}F_1(x,Q^2) + \frac{M}{\nu}\cos^2\frac{\theta}{2}F_2(x,Q^2)\right] \tag{2.11}$$

and

$$\frac{d^2\sigma^{\downarrow\uparrow}}{d\Omega dE'} - \frac{d^2\sigma^{\uparrow\uparrow}}{d\Omega dE'} = \frac{16\alpha^2 E'^2\sin^2\frac{\theta}{2}}{MQ^4}\left[\frac{E+E'\cos\theta}{\nu}g_1(x,Q^2) - \frac{Q^2}{\nu^2}g_2(x,Q^2)\right] \tag{2.12}$$

where $\sigma^{\downarrow\uparrow}$ and $\sigma^{\uparrow\uparrow}$ are cross sections of the beam and target spin anti-parallel and parallel respectively. Experimentally, one often measures the asymmetry

$$A_{||} = \frac{\frac{d^2\sigma^{\downarrow\uparrow}}{d\Omega dE'} - \frac{d^2\sigma^{\uparrow\uparrow}}{d\Omega dE'}}{\frac{d^2\sigma^{\downarrow\uparrow}}{d\Omega dE'} + \frac{d^2\sigma^{\uparrow\uparrow}}{d\Omega dE'}} = \frac{d\sigma^{\downarrow\uparrow} - d\sigma^{\uparrow\uparrow}}{d\sigma^{\downarrow\uparrow} + d\sigma^{\uparrow\uparrow}} \tag{2.13}$$

since this expression can be evaluated using the measured count rates for anti-parallel and parallel spin and the often difficult to determine absolute luminosity and acceptance cancels. This is the approach taken in the present analysis.

2.2 Virtual Photon Asymmetries and Spin Structure Functions

Spin dependent structure functions g_1 and g_2 can be measured in inclusive polarized lepton scattering from a polarized target. The same reaction can also be analyzed in terms of virtual photon absorption cross section. In the electron scattering experiment, the

electron emits a virtual photon γ^* and the virtual photon is absorbed by the nucleon. Virtual photons can have 3 possible spin states which are $m = 0$ (longitudinal) and $m = \pm\ 1$ (transverse). The cross section for the unpolarized case can be separated into two parts, a transverse photon part σ_T ($m = \pm\ 1$) and a logitudinal) photon part σ_L ($m = 0$) :

$$\frac{d\sigma}{d\Omega dE'} = \Gamma_T \sigma_T(\gamma^*) + \Gamma_L \sigma_L(\gamma^*) \tag{2.14}$$

These cross sections are related to the transverse and longitudinal structure functions $W_1 = F_1/M$ and $W_L = (1+\tau)W_2 - W_1$ where $\tau = \nu^2/Q^2$,

$$\sigma_T\,(\gamma^*) = \frac{4\pi^2\alpha W_1}{K} \tag{2.15}$$

$$\sigma_L\,(\gamma^*) = \frac{4\pi^2\alpha W_L}{K} \tag{2.16}$$

and $K = (W^2 - M^2)/2M = \nu - Q^2/2M$ is the equivalent energy for a real photon to reach the same final state invariant mass W (Hand convention). The ratio of the two photon polarization states can be written as $\Gamma_L = \epsilon\Gamma_T$ using $\epsilon = (1 + 2(1+\tau)\tan^2(\frac{\theta}{2}))^{-1}$. Eq. 2.14 can be written again as

$$\frac{d\sigma}{d\Omega dE'} = \Gamma_T \sigma_T(\gamma^*)(1 + \epsilon R). \tag{2.17}$$

where R is the ratio of longitudinal to transverse photoabsorption cross sections, $R = \sigma_L/\sigma_T$.

If the incident (virtual) photon and the target are polarized either parallel or anti-parallel, the total spin of the final hadronic state along the photon direction can be either $S_z = \pm 3/2$ or $S_z = \pm 1/2$ depending on the orientation of target and photon helicity (Fig.2.2). The photon asymmetries A_1 and A_2 can be defined in terms of the corresponding (virtual) photon absorption

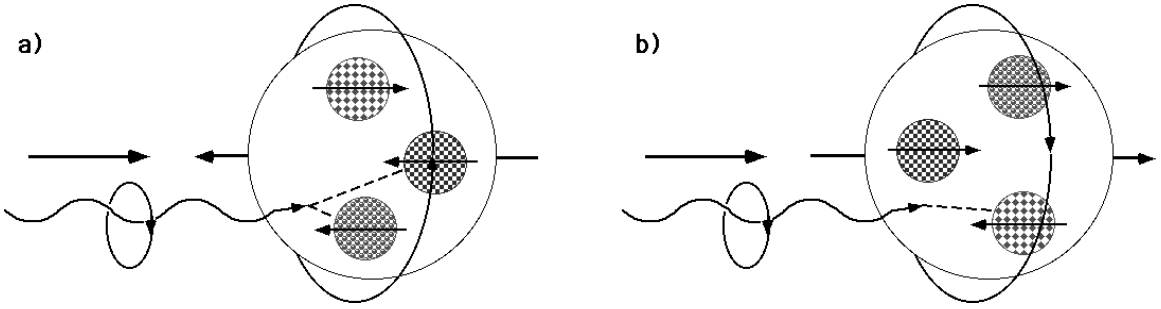

Figure 2.2: Polarized virtual photon absorption on quarks inside nucleons. One can see that only quarks with their spin parallel to the overall nucleon spin can contribute to $\sigma_T^{1/2}(\gamma^*)$ (a), while quarks with their spin opposite to the nucleon spin contribute to $\sigma_T^{3/2}(\gamma^*)$ (b). The virtual photon has positive helicity ($s_z(\gamma^*) = +1$) in these sketches.

cross sections,

$$A_1(\gamma^*) = \frac{\sigma_T^{1/2}(\gamma^*) - \sigma_T^{3/2}(\gamma^*)}{\sigma_T^{1/2}(\gamma^*) + \sigma_T^{3/2}(\gamma^*)} \tag{2.18}$$

and

$$A_2(\gamma^*) = \frac{\sigma_{TL}}{\sigma_T} \tag{2.19}$$

where σ_{TL} is the longitudinal-transverse interference cross section.

A measurement of A_1 in the resonance region can provide a direct tool to study the spin properties of the electromagnetic transition form factors for the baryon resonances. In elastic scattering, the final state is a spin-1/2 state and $|S_z| = 3/2$ is excluded, $\sigma_T^{3/2}(\gamma^*) = 0$ and $A_1 = 1$. On the other hand, the Δ ($P_{33}(1232)$) resonance has spin 3/2. Therefore both $|S_z| = 3/2$ and $|S_z| = 1/2$ final states are possible. According to the Clebsch-Gordon coefficients (assuming a pure M1 transition), the cross section $\sigma_T^{1/2}(\gamma^*)$ is only 1/3 the size of $\sigma_T^{3/2}(\gamma^*)$ which yields $A_1 = -1/2$. For another example, the $P_{11}(1440)$, the Roper resonance, is a spin 1/2 resonance which will lead to a more positive overall value of A_1 than

that for the Δ alone in the region where both resonances overlap. Measurements of A_1 across the resonance region can help unravel the relative strength of these and other partially overlapping resonances and the non-resonant background. The Q^2 dependence of these asymmetries sheds light on the resonance transition form factors. Additional information can be extracted from a comparison of proton and neutron asymmetries, especially on the isospin decomposition of each transition. This is one of major motivations of the present experiment on the deuteron.

The experimental asymmetry $A_{||}$ introduced earlier can be written in terms of the two virtual photon asymmetries A_1 and A_2:

$$A_{||} = \frac{d\sigma^{\downarrow\uparrow} - d\sigma^{\uparrow\uparrow}}{d\sigma^{\downarrow\uparrow} + d\sigma^{\uparrow\uparrow}} = D(A_1 + \eta A_2) \tag{2.20}$$

with the following definitions:

$$D = \frac{1 - \epsilon E'/E}{1 + \epsilon R} \tag{2.21}$$

$$\eta = \frac{\epsilon\sqrt{Q^2}/E}{1 - \epsilon E'/E} \tag{2.22}$$

To extract A_1 from these measurements, one has to know the values of R and A_2 which are presently not well known in the resonance region. The correction due to R is fairly minor, but since η is not small in our experiment, the uncertainty due to A_2 can be substantial, and we only quote our results for $A_1+\eta A_2$. In principle, A_1 and A_2 can be separated by measuring both with longitudinal and with transverse target spin, or by varying the kinematic factors D and η at fixed ν and Q^2 (Super-Rosenbluth separation). The first method is not possible with the CLAS detector since the beam would be deflected too much by the target magnet, and the second method requires much higher statistics than we were able to collect in the present experiment.

The spin structure functions g_1 and g_2 can also be defined in terms of the asymmetries A_1 and A_2 as

$$g_1(x,Q^2) = \frac{\tau}{1+\tau}\left(A_1(x,Q^2) + \frac{1}{\sqrt{\tau}}A_2(x,Q^2)\right)F_1(x,Q^2) \quad (2.23)$$

and

$$g_2(x,Q^2) = \frac{\tau}{1+\tau}\left(\sqrt{\tau}A_2(x,Q^2) - A_1(x,Q^2)\right)F_1(x,Q^2). \quad (2.24)$$

Inverting Eq.2.20 and inserting in Eq.2.23 yields

$$g_1(x,Q^2) = \frac{\tau}{1+\tau}\left(A_{||}/D + \left(\frac{1}{\sqrt{\tau}} - \eta\right)A_2(x,Q^2)\right)F_1(x,Q^2) \quad (2.25)$$

Due to the partial cancellation of the two terms in front of A_2, its uncertainty has less impact in this case and we can use a model for A_2 to extract g_1 from our data.

In the resonance region, g_1 can be linked to the spin-dependent transition strength for different resonances. On the other hand, in the deep inelastic (scaling) limit ($\tau \to \infty$), g_1 converges to $g_1(x) \to A_1(x)F_1(x)$ since $|A_2|$ is bounded by $\sqrt{R}$ which disappears in this limit. This allows us to interpret g_1 in terms of quark distribution functions.

2.3 The Quark Spin Distribution

The simplest version of the constituent quark model[3] describes the nucleon as the ground state of three quarks in a symmetrical S-state and the resonances as excited states in a harmonic oscillator potential. One can define the distribution function $q_i(x)$ as the probability density of finding a given quark flavor i with momentum fraction x inside the nucleon. The spin dependent structure function g_1 can be written using the distribution functions $q_i^{\uparrow\downarrow}(x)$

with two different polarization directions, parallel or anti-parallel to the nucleon spin.

$$g_1(x) = \frac{1}{2}\Sigma_i e_i^2 \left(q_i^{\uparrow}(x) - q_i^{\downarrow}(x)\right) \tag{2.26}$$

where e_i is the individual parton's charge. The net spin contribution of a quark flavor i can be defined as

$$\Delta q_i = \int_0^1 \left[q_i^{\uparrow}(x) - q_i^{\downarrow}(x)\right] dx \tag{2.27}$$

The non-zero matrix elements of the axial-vector current operator are a singlet contribution a_0 and non-singlets a_3 and a_8.

$$a_0 = \Delta\Sigma = \Delta u + \Delta d + \Delta s \tag{2.28}$$

$$a_3 = F + D = \Delta u - \Delta d \tag{2.29}$$

$$a_8 = 3F - D = \Delta u + \Delta d - 2\Delta s \tag{2.30}$$

The matrix elements a_3 and a_8 can be determined by the weak decay constants, F and D, which are constrained by hyperon and neutron beta decay measurements. The integral over the spin strucure function $g_1(x)$ (Ellis-Jaffe integral) leads us to the spin probabilities weighed with the squared quark charges.

$$\Gamma_1^p = \int_0^1 g_1^p(x)dx = \frac{1}{2}\left(\frac{4}{9}\Delta u + \frac{1}{9}\left[\Delta d + \Delta s\right]\right) \tag{2.31}$$

$$\Gamma_1^n = \int_0^1 g_1^n(x)dx = \frac{1}{2}\left(\frac{4}{9}\Delta d + \frac{1}{9}\left[\Delta u + \Delta s\right]\right) \tag{2.32}$$

Using the values extracted from beta-decays, $\Delta u - \Delta d = 1.26$ and $\Delta u + \Delta d - 2\Delta s = 0.58$, and assuming $\Delta s = 0$, one can predict [4] values of the integral $\Gamma_1^p = 0.186$ for protons and $\Gamma_1^n = -0.024$ for neutrons. But the data show different answers from this prediction by Ellis and Jaffe, about 0.14 for the proton and -0.06 for the

neutron, yielding a quark contribution $\Delta\Sigma = \Delta u + \Delta d + \Delta s \approx .25 \pm .05$ to the overall proton spin and implying that a part of the proton spin is carried by the orbital angular momentum of the constituents and an additional contribution comes from the gluonic field. The polarized distributions can be expressed in terms of the contribution from valence and sea quarks ($\Delta\Sigma$), gluons (ΔG) and the total orbital angular momentum of the nucleon constituents (L_z).

$$J_z = \frac{1}{2}\Delta\Sigma + \Delta G + L_z = \frac{1}{2} \tag{2.33}$$

where $\Delta G = G^+ - G^-$ is the difference between the helicity parallel and anti-parallel gluon distributions within the nucleon. Existing data imply that the valence quark contribution is close to (relativistically corrected) expectations, while the sea is negatively polarized and the gluons contribute a significant and likely positive amount. On the other hand, the role of the orbital angular momentum is still unknown so far.

The difference between the proton and the neutron integral, the Bjorken sum rule [5], is more fundamental since the contribution of strange quarks is cancelled and only isospin symmetry is invoked:

$$\Gamma_1^p - \Gamma_1^n = \frac{1}{2}\left(\frac{3}{9}\Delta u - \frac{3}{9}\Delta d\right) = \frac{1}{6}(\Delta u - \Delta d) = \frac{1}{6}g_A \tag{2.34}$$

where g_A is the axial coupling constant in neutron beta decay. At finite Q^2, QCD predicts a logarithmic Q^2 dependence of all structure functions due to the 'running' of the coupling constant $\alpha_s \approx 1/\log(Q^2)$ and gluon radiative effects. The Bjorken sum rule including corrections to order α_s^3 can be written [6] as:

$$\int_0^1 \left[g_1^p(x,Q^2) - g_1^n(x,Q^2)\right] dx = \frac{g_A}{6}\times$$
$$\left[1 - \frac{\alpha_s(Q^2)}{\pi} - 3.5833\left(\frac{\alpha_s(Q^2)}{\pi}\right)^2 - 20.2153\left(\frac{\alpha_s(Q^2)}{\pi}\right)^3 \cdots\right] \tag{2.35}$$

All existing data confirm the integral value 0.21 with perturbative QCD corrections. Similar pQCD corrections apply to the integrals for the proton and the neutron separately.

2.4 Q^2 dependence of the spin structure functions

In the QCD-improved parton model, the quark distributions and spin structure functions evolve with Q^2 due to gluon bremsstrahlung and gluon-induced quark-antiquark pair creation. QCD predicts that the number of resolved partons which share the nucleon's momentum increases with Q^2. The probability of finding a quark is increased at small x and is decreased at large x because high momentum quarks lose momentum by radiating gluons. The evolution of the parton distribution with Q^2 produces the logarithmic Q^2 dependence of the polarized and unpolarized structure functions. The Q^2 evolution of structure functions is theoretically described using NLO (next to leading order) analysis based on the Dokshitzer-Gribov-Lipatov-Altarelli-Parisi (DGLAP) evolution equations [7,8,9]. The DGLAP equations show that the Q^2 dependence of the quark distribution is related to the gluon polarization, which can therefore in principle be inferred from measurements of spin structure functions over a large kinematic regime. Unfortunately, the present data set on the deuteron is too restricted in kinematic range to contribute significantly to the world data in the deep inelastic region in this respect.

The evolution of the unpolarized and polarized structure functions is similar and the ratio g_1/F_1 (or the asymmetry A_1) could depend much less on Q^2. This is indeed born out by results from experiment E143 [11] at SLAC which show that above $Q^2 \approx 1$ GeV^2, this ratio is nearly independent of Q^2. However, below 1 GeV^2 the Q^2 dependence of the ratio g_1/F_1 becomes stronger, possibly due to higher twist effects. Higher twist contributions basically stem from inteference terms between different quark currents as

well as quark-gluon correlations and final state interactions of the struck quark. These higher twist effects [10] yield corrections to the structure functions proportional to powers of $1/\sqrt{Q^2}$ and recent data [11] indicate that higher twist may change the proton integral by as much as 3% - 5% at $Q^2 = 3$ GeV^2. As nucleon resonances become more important (at lower W and Q^2), the structure functions and asymmetries are mostly driven by the resonant final state. As Q^2 decreases, the asymmetries become less positive and eventually change sign, in particular in the region of the Δ resonance. Correspondingly, the integrals Γ^p and $\Gamma^d \approx \Gamma^p + \Gamma^n$decrease rapidly and become negative as Q^2 approaches zero. The energy scale at which the resonant final states become important coincides with a resolution $1/Q^2$ appropriate for the size of the constituent quarks. We cannot directly measure the "constituent quark distribution function" without considering the final hadronic state. However, the measured structure functions averaged over several resonant final states may still agree with the ones measured in the deep inelastic region after the proper extrapolation to the resonace region, as has been shown in the case of unpolarized structure functions [12] (*local duality*). It is still an open question whether (and how well) duality works in the case of polarized structure functions [13,14]. Our data allow a first test of duality for the case of g_1^d of the deuteron. In general, our data can be compared to models (see, e.g., Ref. [15]) that attempt to describe the transition between the perturbative QCD description of spin structure functions (including higher twist) and the limit of strong coupling QCD at low Q^2 and in the resonance region.

2.5 Gerasimov-Drell-Hearn Sum Rule

In 1966, S.B. Gerasimov [17] and separately S.D. Drell and A.C. Hearn [18] derived a sum rule which relates the spin-dependent total cross section of circularly polarized real photons on longitudinally

polarized nucleons to the anomalous magnetic moment of the nucleon. The GDH sum rule is:

$$I^{GDH} = \frac{m^2}{8\pi^2\alpha}\int_{\nu_{thr}}^{\infty}\left(\sigma_{1/2}-\sigma_{3/2}\right)\frac{d\nu}{\nu} = -\frac{\kappa^2}{4} \tag{2.36}$$

where $\sigma_{1/2}$ and $\sigma_{3/2}$ are the total cross section for hadron photoproduction for total helicity $\frac{1}{2}$ and $\frac{3}{2}$, κ is the anomalous magnetic moment of the nucleon, ν is the lab energy of the photon and ν_{thr} is the pion photoproduction threshold energy. This sum rule is derived from two theorems, the low energy theorem [19,20] and the dispersion relations [21] for forward Compton scattering. Since no assumptions were made using QCD or the parton model, the GDH sum rule is considered to be sturdy and could provide a good check point on various nucleon models, as well as the behavior of $\Gamma_1^p(Q^2)$ and $\Gamma_1^n(Q^2)$ as $Q^2 \to 0$. However, some recent analyses of pion photo-production amplitudes [22,23,24] claim that the sum rule may be violated, especially if one considers the difference between the proton and the neutron result. In principle, such a violation could indicate that the "no subtraction" assumption for the integral is invalid. However, a more likely scenario is that there are significant other contributions to the integral (from multi-pion production, eta and other meson production, and from the high-energy region beyond $W = 2$ GeV), which are not properly included in the evaluation of Refs. [22,23,24].

The GDH sum rule for the proton can be tested against recent measurements at MAMI [25] and ELSA which agree well with the sum rule prediction. A direct measurement for the neutron is still outstanding. However, by measuring the spin structure function integrals Γ_1 at small Q^2, one can constrain the value of the real photon integral. To connect the integrals Γ_1 to the GDH integral, one can use the relationships quoted in Section 2.2 to show [26] that

$$\Gamma_1^N(Q^2 \to 0) \to \frac{Q^2}{16\pi^2\alpha}\int_{\nu_{thr}}^{\infty}\left(\sigma_{1/2}-\sigma_{3/2}\right)\frac{d\nu}{\nu} = -\frac{Q^2}{8M^2}\kappa_N^2. \tag{2.37}$$

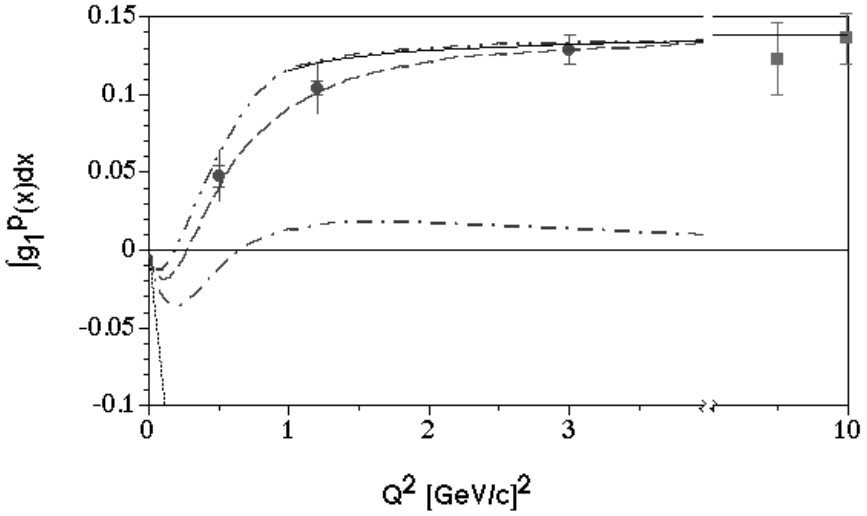

Figure 2.3: The first moment of the proton spin structure function g_1. The data shown are SLAC (circle) and CERN (rectangle) data. The solid line at higher Q^2 is the Q^2 evolution of the integral in the DIS domain. The dotted line at $Q^2 \to 0$ indicates the slope predicted by the GDH sum rule. The other lines are predictions from, from the top, Soffer/Teraev, Burkert/Ioffe and Burkert(from AO, resonance only). Details are in the text.

Since the GDH sum rule is negative, the integrals $\Gamma_1^{p,d}(Q^2)$ must have a negative slope at $Q^2 = 0$ and then change rapidly at low Q^2 to meet the positive experimental results in the DIS region. This low-Q^2 behavior is dominated by the contribution from the Δ and, to a lesser extend, other resonances.

2.6 Theoretical Predictions of the Spin Structure Functions and the Sum Rules

Theoretical calculations and models for the spin structure functions and sum rules have been made by several groups. For the proton, the GDH sum rule predicts a negative slope at $Q^2 \approx 0$ for the value of the integral Γ_1^p while all experiments yield positive values in the

DIS domain. Fig.2.3 shows the rapid change and zero-crossing at $Q^2 < 1$. The SLAC (E143) data indicate that the integral starts decreasing rapidly as Q^2 decreases. The zero-crossing, however, is still not confirmed and more precise data, also covering the lower Q^2 region, are needed. The Q^2 dependence of the sum rule was first parametrized by Anselmino and others [26] using a model based on the vector meson dominance which describes $\Gamma_{p,n}(Q^2)$ throughout the whole Q^2 region. Burkert and Li [27] have parametrized the amplitudes for the resonances up to 2 GeV using existing experimental data. They see a strong Q^2 dependence of the resonance contributions which, by themselves, would change the sign of the proton integral at $Q^2 \approx 0.8$ GeV^2. Burkert and Ioffe [28] then combined the contribution from the resonances with a smooth parametrization of the non-resonant part, following the ansatz of Anselmino. The parametrization is chosen such that both the GDH integral is recovered in the limit $Q^2 \to 0$ and the measured value for the integral Γ_1 is reproduced in the DIS region. Soffer and Teryaev [29] suggested that the rapid change of the Γ_1 at low-Q^2 region is determined by the Burkhardt-Cottingham sum rule.

$$\int_0^1 dx g_2(x, Q^2) = 0 \tag{2.38}$$

The sum $\Gamma_1 + \Gamma_2$ is related to the longitudinal-transverse inteference cross section σ'_{LT} and the rapid fluctuation of Γ_1 follows by subtraction of the Burkhardt-Cottingham sum rule value of Γ_2. Recently, Ji and Osborne [30] evaluated the Q^2 dependence of the GDH sum rule using chiral perturbation theory at $Q^2 = 0$ to 0.2 GeV^2 and the twist-expansion (OPE) from $Q^2 = \infty$ to about 0.5 GeV^2 providing constraints on the Q^2 evolution of the sum rule at both low and high Q^2. Drechsel and others [31] calculated the spin structure functions g_1 and g_2 using a model based on a gauge-invariant and unitary isobar model for one pion photo- and electroproduction. They found that the zero-crossing of the proton integral Γ_1 shifts from $Q^2 = 0.75$ GeV^2 (for the single pion channel only) to

$Q^2 = 0.45$ GeV^2 when they include η and multi-pion channels. Inclusive spin structure function data, SLAC E130 [35] and E143 [36], show the asymmetry in the resonance region of the Δ region is indeed negative and compatible with $A_1 = -0.5$ but the integral stays positive above $Q^2 \approx 0.5$ GeV^2. An accurate measurement of the spin structure functions at low Q^2 is needed for a better understanding of higher twist and nonperturbative contributions to the structure functions.

2.7 Spin Structure Functions of the Deuteron

It is important to study the spin structure functions (g_1) and their integrals (Γ_1) for both the proton and the neutron to unravel the isospin-dependence of quark distributions (Δu *vs.* Δd) and resonance transitions. In particular, the integral $\Gamma_1^p - \Gamma_1^n$ offers a unique opportunity to test models of the nucleon over the whole range of resolution (Q^2) since exact sum rules exist both in the limit of high Q^2 (the Bjorken sum rule) and at $Q^2 = 0$ (the GDH sum rule). On the other hand, the isoscalar integral $\Gamma_1^p + \Gamma_1^n$ provides a particularly strong constraint on the net quark polarization, $\Delta\Sigma = \Delta u + \Delta d + \Delta s$, since the contribution to this integral due to strange quarks is small and only the combination $3F - D$ is needed as external input (see Section 2.3).

In the absence of a free neutron target, spin structure functions of the neutron have to be extracted from measurements on the deuteron or ^{3}He. Both targets have been used in past measurements in the DIS region at SLAC [32,33] and HERMES [34] as well as for measurements in the resonance region at Jefferson Lab (including the present data). Since nuclear corrections are quite different for these two targets, a comparison of the extracted neutron spin structure functions from both can test how well we control these nuclear corrections. This is particularly important for measurements in the resonance region, where corrections like resonance broadening due

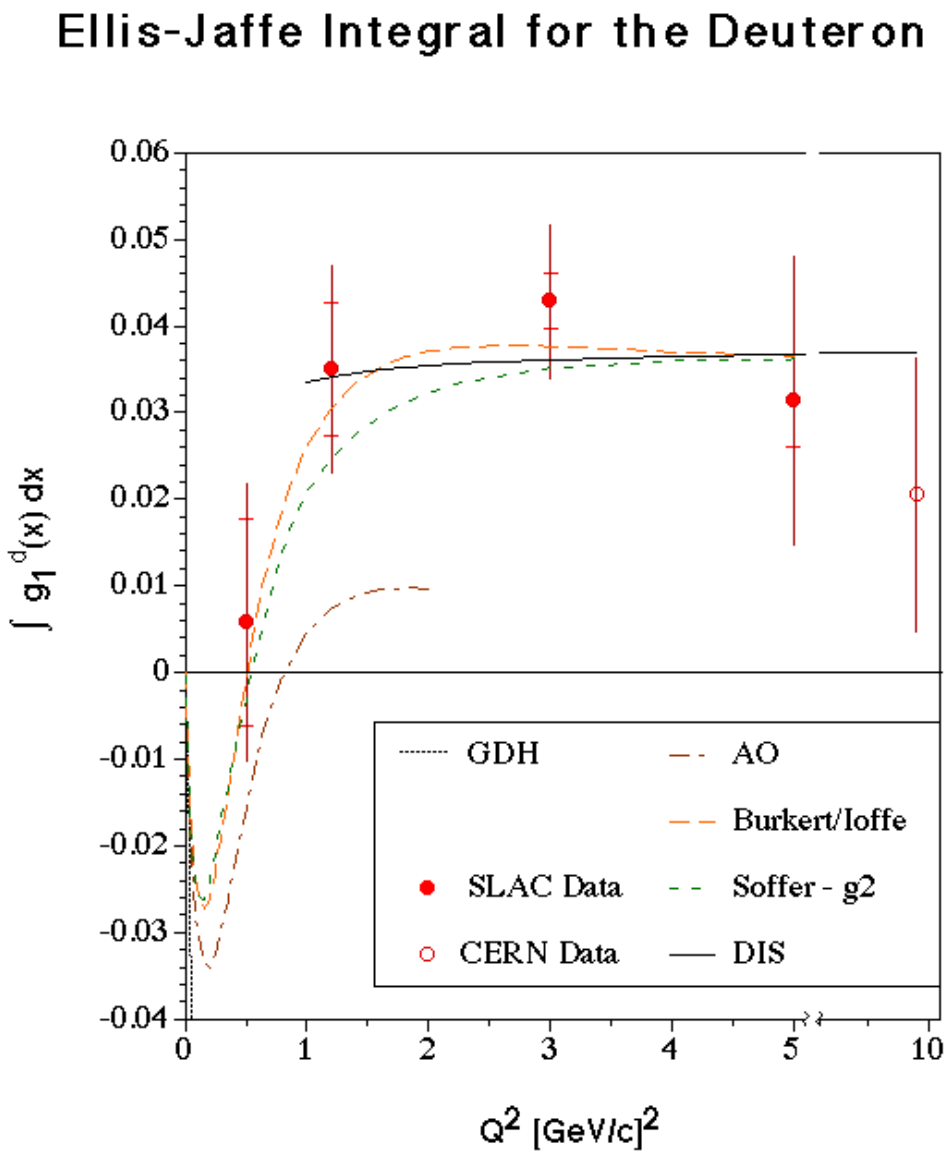

Figure 2.4: Ellis-Jaffe Integral for the Deuteron. SLAC data and theoretical predictions

to Fermi motion could play a much more important role than in the DIS regime. The advantage of using ^{3}He as a "neutron target" lies in the relatively small contribution from the protons in ^{3}He since in the ground state they are mostly coupled to a spin-0 pair. On the other hand, the deuteron is a more loosely bound system of only two nucleons, and nuclear effects like Fermi-motion, binding (off-shell) effects, meson exchange currents, final state interactions, nuclear shadowing, non-nucleonic components in the wave function and coherent meson production are both smaller and can be more realistically modelled with state-of-the art relativistic calculations (see, e.g., references [37,39,40]). In particular the integral Γ_1^d over the deuteron spin structure function g_1^d is very close to the isoscalar integral $\Gamma_1^p + \Gamma_1^n$, with only minor corrections due to the deuteron D-state:

$$\Gamma^D(Q^2) \approx \left(1 - \frac{3}{2}P_D\right)\left(\Gamma^n(Q^2) + \Gamma^p(Q^2)\right)/2 \qquad (2.39)$$

where $P_D \approx 5\%$ is the weight of the D-wave in the deuteron. Corrections to this relationship are estimated [39] to be less than 3% for $0.1 < Q^2 < 2.0$ GeV^2.

Additional information on nuclear effects can be gotten from a comparison of the GDH sum rule prediction for the deuteron as a whole to the sum of the predictions for the proton and neutron individually. The anomalous magnetic moments for proton and neutron result in the GDH integral value $I_p^{GDH} = -204.8\mu b$ for the proton and $I_n^{GDH} = -233.2\mu b$ for the neutron. Thus, the GDH prediction for the incoherent sum of proton and neutron integrals is about $-438\mu b$. On the other hand, the experimental value of the anomalous magnetic moment for the deuteron is very small, $\kappa_d = -0.143$, resulting in the GDH prediction $I_d^{GDH} = -0.65\mu b$ where the integral is to be taken from the threshold of *nucleonic* breakup of the deuteron (2.22 MeV) to infinity. To satisfy this small value on the deuteron GDH integral, a large positive contribution to the integral is needed below pion threshold. Arenhovel

et. al. [40] evaluate this part of the GDH sum rule for the deuteron by explicit integration up to a photon energy of 550 MeV, including photodisintegration channels as well as coherent and incoherent single pion photoproduction channels. The contribution from photodisintegration ($\gamma d \to np$) is dominantly from the $M1$ transition to $^1S_0$ at very low energy, which can only be reached by the antiparallel spin orientation, resulting in a large positive contribution to the deuteron GDH integral. This contribution nearly cancels the incoherent sum of the proton and neutron integrals, implying that nuclear corrections above pion threshold are small. Indeed, the authors of Ref. [40] show that the contribution from incoherent pion production on the deuteron ($\gamma d \to \pi NN$) is very close to the sum of the free proton and neutron values.

Chapter 3

Analysis

The present analysis is based on the data set collected during the first run of the EG1 run group in Hall B in 1998 (EG1a) for experiment 93-009. A polarized solid state target of frozen deuterated ammonia ($^{15}\mathrm{N}\vec{\mathrm{D}}_3$) immersed in a 1 K liquid ^{4}He bath and surrounded by a 5 T superconducting Helmholtz magnet (with better than 10^{-4} field uniformity) was installed inside the CLAS detector (at a position about 57 cm upstream of the nominal CLAS center). The target material was pre-irradiated before the run and polarized by driving a hyperfine transition with 140 GHz microwave radiation (Dynamic Nuclear Polarization). The polarization was monitored using standard NMR techniques throughout the run. A more precise offline determination of the polarization (see Section 3.4) showed that it fluctuated between 0.15 and 0.26. This polarization was lower than usually obtainable with this method (0.3 - 0.4) due to insufficient microwave power and less than optimal target material. The direction of the target polarization was along the beam direction. A small sample of runs was taken with opposite target polarization, but this sample was not used in the present analysis due to its low target polarization and low statistics. The total target thickness was about 1 g/cm^2, about 65% of which

came from the ammonia, while the rest was made up of LHe coolant and various entrance and exit foils and heat shields (Kapton and Aluminum). Additional runs were taken on an empty target cell (immersed in the same liquid He bath) and on a cell containing a slab of ^{12}C of the same thickness in g/cm^2 as the ammonia ("Carbon target"). These runs were used to extract the dilution of the desired asymmetries through unpolarized nucleons in the ammonia targets.

Polarized electrons from the CEBAF strained GaAs cathode were accelerated to 2.5 GeV or 4.2 GeV and scattered off this target. The polarization was reversed every second, with a pseudo-random pattern, to ensure cancellation of systematic errors. The beam current was integrated over each 1 second period using a Faraday cup with charge-to-pulse converter which yielded a count ("click") for each 0.1 nC of integrated charge in a helicity-gated scaler. Substantial differences between the current for positive and negative beam helicity were found (of order 0.3%) which made accurate normalization of the physics count rates very important. The beam was rastered over part of the target cross section to avoid local depolarization; unfortunately, a substantial target misalignment prevented us from illuminating the whole target uniformly, which contributed to the low target polarization and made the NMR measurements rather unreliable. Only very few runs were taken with 4.2 GeV electrons on ND_3, which were excluded from the present analysis due to their low statistics. The 2.5 GeV runs fell into two categories: Most were taken with the CLAS in its nominal "electron inbending" (positive) torus polarity, with an average beam current of about 2.5 nA (total luminosity about 9×10^{33}) and an average beam polarization of about 0.71, as measured during periodic runs with the Hall B Moller polarimeter. Some runs were also taken with the CLAS torus in "outbending" (negative) polarity. However, the beam current for these runs had to be reduced to about 0.5 nA, leading to unstable beam and large normalization

errors (since the Faraday cup electronics yielded only 5 "clicks" for each 1 second helicity state at these low currents). A statistical analysis of two sets of these runs taken at different dates (about 1 month apart) showed that they were mutually inconsistent (possibly because the target material had been changed in between). Since they also had low statistics, it was decided to omit them from the final analysis reported here.

The scattered electrons were detected in the CLAS detector with its usual configuration, except that the mini-torus was removed to make room for the polarized target and a special downstream beamline with lead shielding was introduced. The 5 T field of the target provided sufficient shielding against Moller electrons. The large acceptance of CLAS more than offset the relative small luminosity that can be achieved with solid state polarized targets, and it allowed us to cover the whole kinematic range from elastic scattering to the edge of the resonance region (W = 2GeV) and from Q^2 = 0.3 GeV/c^2 to 1.2 GeV/c^2.

3.1 Raw Data Analysis

The data analysis is based on the standard Hall B analysis package, RECSIS release-1-21. RECSIS consists of individual detector analysis packages and packages to combine those information and to reconstruct particle tracks and particle identification. The raw data from all CLAS experiments stored on tape (STK Redwood tape drive controlled by the Mass Storage Server) in BOS format, Fig.[3.1]. BOS is a program system written in FORTRAN 77 for the dynamic management of data. In this dynamic memory management system, the data areas are called *banks* and each bank contains *data*. All banks are stored in one large COMMON area. The Hall B DAQ system (CODA) separates data in runs and files. Each file has maximum size of 2 GByte and one run has about 10 to 20 files. Data contain the raw detector events, mainly TDC

and ADC values from each detector as well as beam related information. RECSIS converts these raw data into meaningful physics quantities (a process called *cooking*). About 10% of the data were processed during the first part (pass 0) of processing for detector calibrations and general quality checks. The pass 0 data sample was selected evenly throughout the entire running period, considering running conditions and experiment downtime. The very first run of each running period is also included for the detector calibration. The full data processing was done using the JLab Linux batch farm from August to October 1999. The monitoring and quality checks were done online and offline during the processing. Monitoring histograms for each detector component and for reconstructed physical variables were written and monitored on a file-by-file basis. A web-based database was used for the quality bookkeeping, identifying reconstrucion and hardware failures. Ntuples were generated from the processed data. These ntuples only contain variables necessary for the physics analysis.

The event selection and particle identification are described in Section 3.2. Due to the uncertainties on the magnetic field and detector geometry survey, momentum corrections were applied to each electron track, Section 3.3. In Section 3.4, the extraction of the target polarization from the inclusive and exclusive analysis is explained. The dilution factor is described in Section 3.5, and additional backgrounds are discussed in Sections 3.6 and 3.7. After dealing with dead-time corrections (Section 3.8), the extraction of the raw asymmetries is presented in Section 3.9. Radiative corrections and the models that enter them are discussed in Sections 3.10 and 3.11, respectively, followed by a section on electroweak corrections (Section 3.12). The final two sections deal with the extraction of final Physics results (Section 3.13) and a complete discussion of systematic errors (Section 3.14). Additional information on the running conditions, data taken and analysis details can be found in the analysis notes by Raffaella DeVita and Renee Fatemi, as well

as the Ph.D. thesis of Junho Yun.

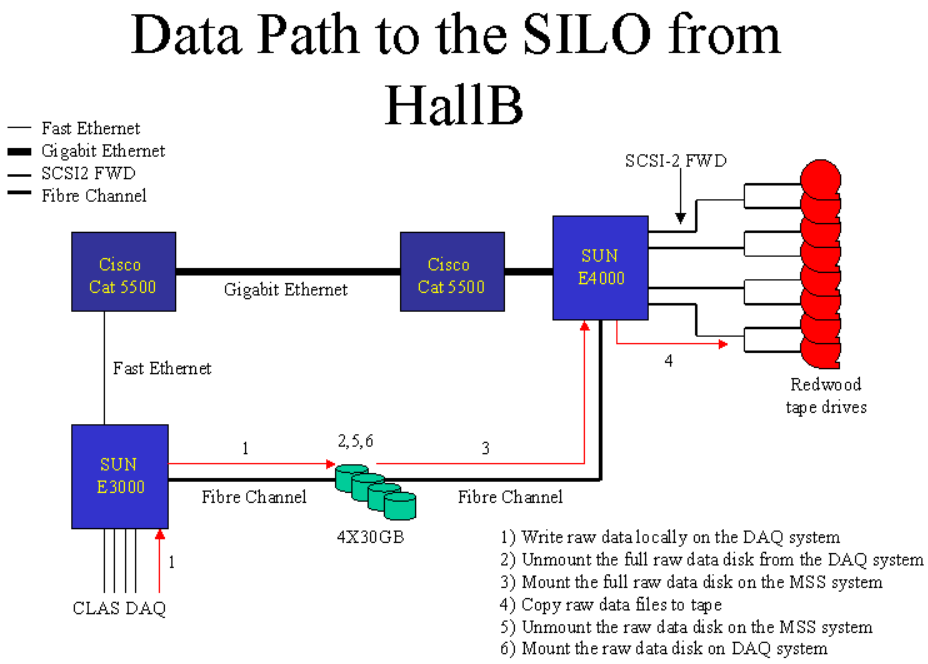

Figure 3.1: The CLAS data flow layout.

3.2 Run/Event Selection

All physical variables for each identified particle track needed for the present analysis, Table [3.1], were written into specialized ntuple files on an event-by-event basis. The total data set consist of 320M electron events at 2.5 GeV for the inbending, positive torus current of 2250 A, and 150M at 2.5 GeV for the outbending, negative torus polarity (-1500 A). The inbending runs were separated into 5 groups and the outbending into 2 groups according to the

event number
particle ID (SEB)
momentum
x vertex
y vertex
z vertex
theta
phi
corrected momentum
2nd moment from EC hit
total energy in EC
inner EC energy
outer EC energy
number of photoelectrons in CC
β
energy in SC
x-coord EC hit
y-coord EC hit
x vertex at DC1
y vertex at DC1
z vertex at DC1
x cosine at DC1
y cosine at DC1
z cosine at DC1
helicity

Table 3.1: The physical quantities stored into ntuples.

group	run number	beam energy (GeV)	torus (A)	target pol.
inbending group1 *	15360 - 15383	2.494	+2250	0.22
inbending group2	15385 - 15388	2.494	+2250	-0.15
inbending group3 *	15389 - 15405	2.494	+2250	0.20
inbending group4 *	15213 - 15235	2.565	+2250	0.26
inbending group5 *	15272 - 15339	2.565	+2250	0.16
outbending group1	15406 - 15421	2.494	-1500	0.19
outbending group2	14629 - 14679	2.565	-1500	0.20

Table 3.2: Runs are separated into inbending (5 groups) and outbending (2 groups) and analyzed separately. The run groups which were included in the final analysis are indicated by asterisks (*)

beam condition, the target polarization (NMR measurements) and the running period, Table [3.2]. For positive torus polarity, electrons bend toward the beamline resulting in a suppression of small scattering angles and, therfore, a better statistics at large θ_e (higher Q^2). The runs with negative torus polarity were not used for the present analysis, as discussed above, except to study the longterm trend in the target polarization.

The "2.5 GeV" data were taken at two slightly different energies, 2.565 GeV and 2.494 GeV, in order to compromise with Hall A and C for high beam polarization ("magic" energy setting). All runs which were taken during major detector breakdowns were excluded from the analysis as well as runs with wrong trigger setup, unstable beam conditions, wrong helicity information and large Faraday cup asymmetries.

Since we measure asymmetries, electrons are separated into two different helicity states. During each run, the electron helicity was chosen at the injector each second. The helicity pattern Fig. [3.2] is formed by pairs of electron buckets with opposite helicity states. A 'Sync' pulse line generates a helicity pulse at 1 Hz and the helicity

for the next 1 second-period ("1 bucket") is chosen. The first of two consecutive helicity states is chosen pseudo-randomly while the second is its complement. The program "HelP" reads all helicity information from the "HLS" and "TGBI" BOS banks and outputs a helicity table for each file. The helicity table contains helicity information for each bucket, as well as the Faraday Cup readings for the integrated beam charge, the range of event numbers occuring in that bucket, and the number of electrons in each sector. The table starts with the helicity state flag for each state. The original flag is the first state of the helicity pair and assigned '1' if both helicity states are in time and the ROC is synchronized. The second state is a complement and assigned '2' if it is a good complement to the first helicity state. Mismatches between the different scaler readings or other problems detected by "HelP" were flagged with negative numbers. A bad helicity bucket cutoff was made primarily using these original and complement flags, 1 and 2 in sequence for a complete bucket pair. These flags take care of the failures like ROC out of sync, scaler helicity mismatch, TGBI bank misreading, and a significant change in the trigger rate or Faraday cup readout failures. Additional cuts were made requiring a Faraday Cup variation of less than 10% from one 1-second "bucket" to the next and a reasonable numbers of electrons reconstructed in each sector. This requirement helped remove problems stemming from beam instabilities, beam drop outs and scaler malfunction. In all cases, buckets of data and the corresponding Faraday cup readings were removed from the data set in *pairs*, ensuring that only matched pairs of opposite helicity in sequence entered the analysis.

In spite of the helicity cuts, there is a systematic difference in the number of beam electrons (charge) for the two opposite helicity states. The average Faraday Cup asymmetry was 0.3%. These false asymmetries are basically from helicity-correlated asymmetries in the beam current. They were corrected by normalizing all count rates to the beam current for each helicity.

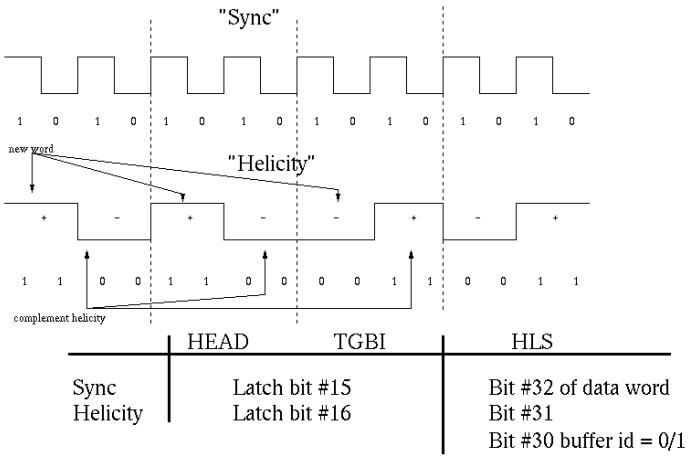

Figure 3.2: The helicity flips at a frequency of 1 Hz with a pseudo-random sequence.

The electron selection is originally from the RECSIS package Simple Event Builder (SEB). Since one negative track is required for the SEB, each event has at least one electron candidate. First, the ideal electron must have a hit in the EC or SC, then the SEB checks the hit position, timing, geometry match for each detector and β using time of flight and momentum analysis. The SEB uses very broad cuts for the initial particle identification.

Additional cuts, Table 3.3, are used for more accurate electron selection. The main source of false electron identification is from e^- and π^- separation, i.e. a π^- misidentified as an electron. These two different particles can be distinguished by their signal in the electromagnetic calorimeter (EC). While most pions deposit only the minimum-ionizing amount of energy in the EC, the electrons shower and deposit nearly all of their energy in the EC. The EC sampling fraction, the fraction of electromagnetic shower energy

1. SEB paricle ID = 11 (electron)
2. Etot/p greater than 0.2 (EC sampling fraction)
3. number of photoelectrons greater than 0.5
4. z vertex from -60cm to -50cm
5. reconstructed radial distance from beam line less than 5 cm
6. electron momentum less than 2.5 GeV
7. electron mementum greater than 0.5 GeV
8. theta less than 50°

Table 3.3: Electron cuts. The norminal target position was -55 cm.

in EC that is detected as scintillation light, is about 0.27. This ratio decreases as the measured electron momentum decreases. A study of the energy calibration shows that the measured electron momentum of 0.5 GeV corresponds to the ratio E_{total}/p of 0.2 where E_{total} is the total energy deposited in both inner and outer EC. Therefore, we identify electrons via a cut that requires the ratio of total energy deposited in the EC and the momentum of a particle to be greater than 0.2 and reject electrons with less than 0.5 GeV momentum.

The Cerenkov counter information is also used in the cut to exclude particles with no associated photoelectron created in CC (the number of photoelectrons required for electrons was greater than 0.5). A more careful treatment of the π^- contamination can be found in Sections 3.7 and 3.14. A vertex cut (reconstructed vertex must be less than 5 cm from the target center) is used to make sure the electron originated from the target (excluding the downstream exit windows and heat shields) and the vertex reconstruction is reasonable. (The target itself was much smaller, 1 cm long and 1.5 cm in diameter. However, due to the limited vertex resolution and the correlation between reconstructed radial and longitudinal position, combined with a lateral offset of the beam and target from CLAS center, the more generous cuts described above had to be

used to avoid losing too many events). No fiducial cuts were used to maximize statistics. While the efficiency of the combined cuts listed in Table 3.3 is not known accurately and can be kinematics-dependent, this efficiency drops out in the calculation of count rate asymmetries. A comparison between the results with and without fiducial cuts showed no statistically significant difference, within the larger error bars of the results with fiducial cuts.

3.3 Momentum corrections

The momentum of a particle is calculated using the drift chamber reconstructed track and the torus magnetic field. However, the knowledge of the drift chamber wire position and the torus magnetic field value is limited due to the accuracy of existing survey data and B field maps. All CLAS data show a systematic shift of the reconstructed electron momentum relative to the expected one in the case of kinematically complete events. These are due to the difference between the actual drift chamber geometry (and torus magnetic field) and survey values parametrized in the reconstruction codes. The correction factor to the electron momentum is extracted comparing the elastic peak position ($W = 0.939$) in the W spectra with the theoretical value and it is a function of ϕ, θ and the torus field, under the assumption that only the momentum is reconstructed incorrectly.

$$P_{correct} = F(\theta, \phi) \cdot \frac{I_0}{I_{read}} \cdot P_{reconstructed} \tag{3.1}$$

$$F(\theta, \phi) = \left(a + b\phi + c\phi^2\right) \frac{d\theta - f}{g\theta - h} \tag{3.2}$$

where $F(\theta, \phi)$ is the correction factor with seven parameters from a fit to the data using a constraint of the corrected position of W elastic peak. I_0 is the actual torus field and I_{read} is the torus field in the database and the one used in the reconstruction. The discrepancy between I_0 and I_{read} stems from inaccurate IOC readout, for

example, the readout torus current I_{read} is $2251A$ while the actual current is $2250A$.

The resulting correction on the electron momentum, Fig 3.3, is of the order of ≈ 0.1 % and tends to decrease for increasing electron polar angle.

3.4 Beam and Target Polarization

The target polarization was measured using the NMR technique during the run. This NMR measurement was not reliable mainly due to the uncertainty on the TE measurement for normalization and the depolarization of the target by the beam. We used alternative methods to extract the product of the target and beam polarization, based on the known asymmetry for elastic scattering off protons and neutrons. This elastic asymmetry is given by

$$A^N_{elastic} = \frac{\cos\psi\sqrt{1-\epsilon^2} + \sin\psi\cos\phi\sqrt{2\epsilon(1-\epsilon)}\left(\frac{Q^2}{4m^2}\right)^{-1/2}\frac{G_E(Q^2)}{G_M(Q^2)}}{1+\epsilon\left(\frac{Q^2}{4m^2}\right)^{-1}\frac{G_E^2(Q^2)}{G_M^2(Q^2)}} \tag{3.3}$$

where the angles $\psi = \theta_q$ and $\phi = 0$ describe the direction of the target spin in relation to the virtual photon and ϵ is the virtual photon polarization parameter. The quantities $G_E(Q^2)$ and $G_M(Q^2)$ are the electric and magnetic (Sachs) form factors of the nucleon in question (proton or neutron), which are known to very good precision in our Q^2 region of interest.

Two semi-independent methods were used to extract the product P_bP_t of beam and target polarization, involving inclusive quasi-elastic and exclusive $(e, e'p)$ events. In the case of the inclusive analysis, one measures the asymmetry in the quasi-elastic peak and compares it to a model calculation which averages the results from Eq. 3.3 over both proton and neutron (weighted by their elastic cross sections) and corrects it for the effects of Fermi motion and the D-state component of the deuteron. The resulting theo-

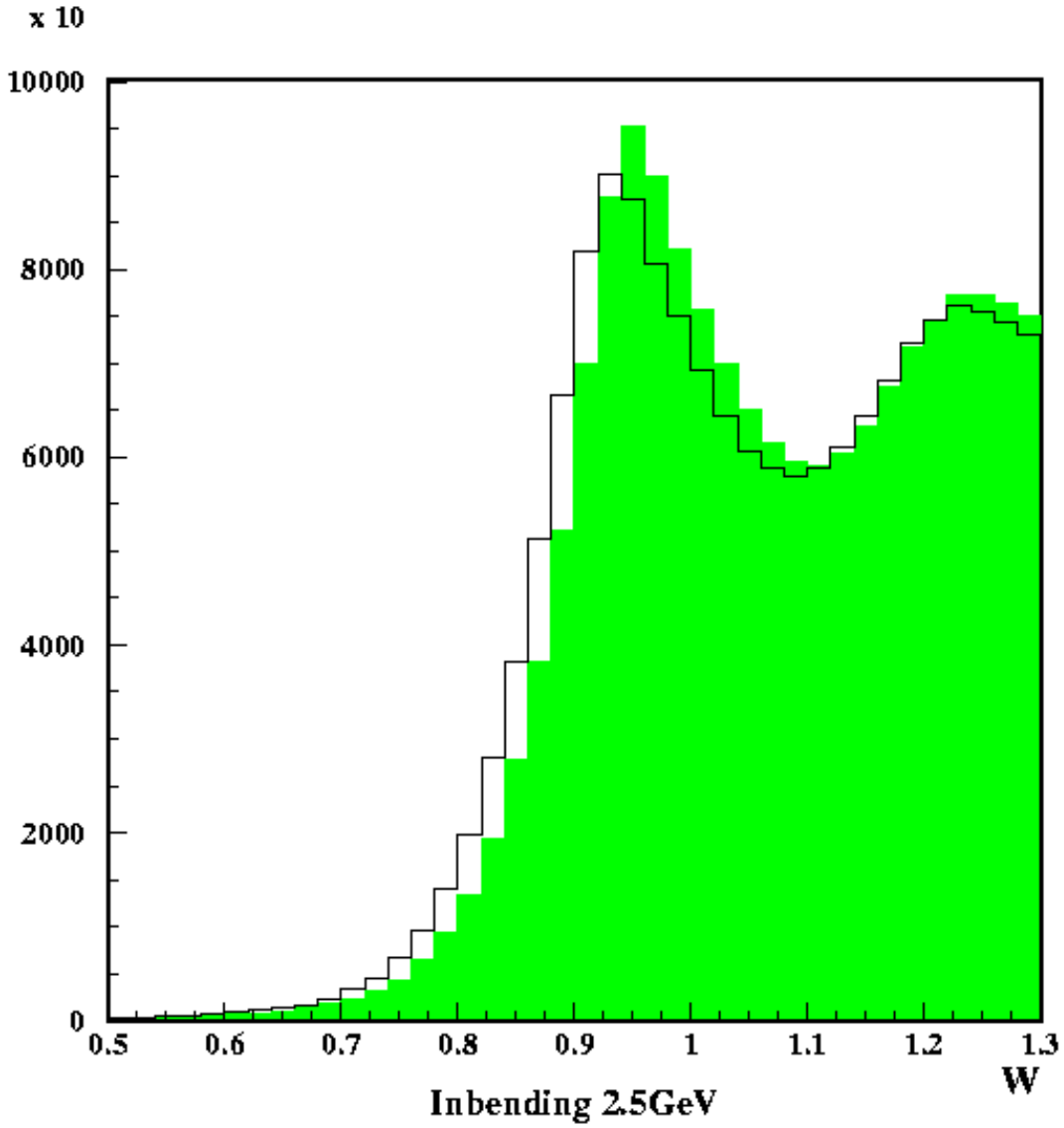

Figure 3.3: W spectra for inclusive electrons before(line) and after(shaded area) the momentum correction. The final width of the quasielastic peak after the correction was 76 MeV. In the case of the corresponding correction on the NH_3 data, the width of the elastic peak was reduced from 23 MeV to 16 MeV.

Q^2	outbending $A_{quasi-elastic}$	inbending $A_{quasi-elastic}$
0.125	0.054	
0.149	0.063	
0.177	0.072	
0.211	0.085	
0.251	0.099	
0.3	0.114	0.113
0.36	0.132	0.130
0.42	0.153	0.153
0.5	0.177	0.177
0.6	0.206	0.206
0.71	0.242	0.242
0.84	0.281	0.281
1	0.330	0.330
1.2		0.390

Table 3.4: The inclusive theoretical asymmetries for the outbending runs up to $Q^2 = 0.36$ GeV^2 have only been integrated from $W = 0.9$GeV^2 - 1.0 GeV^2, while the higher Q^2 bins for the outbending runs and all Q^2 bins for the inbending runs have been integrated over W =0.85 GeV^2 - 1 GeV^2

retical value $A_{quasi-elastic}$, Table 3.4, was calculated in PWIA using up-to-date fits to the nucleon form factors and a Paris potential wave function for the deuteron. The product $P_b P_t$ can be written

$$P_b P_t = \frac{A_{measured}}{DF \times A^d_{quasi-elastic}} \tag{3.4}$$

where DF is the dilution factor due to the presence of unpolarized target material. The evaluation of the inclusive dilution factor will be discussed in the following section. The measured asymmetry was averaged over the region 0.85 GeV^2 $< W <$ 1.0 GeV^2 for all inbending runs and for the outbending events with $Q^2 > 0.4$ GeV^2,

and 0.9 GeV^2 $< W <$ 1.0 GeV^2 for the outbending events with $Q^2 < 0.4$ GeV^2.

In the exclusive method, electron–proton coincidence events in quasi-elastic kinematics were chosen with additional cuts: 0.85 GeV^2 $< W <$ 1.0 GeV^2, $|\theta_p - \theta_{\vec{q}}| < 5^\circ$, 1.3 GeV^2 $< Q^2 <$ 2.0 GeV^2, and $\phi_e - \phi_p = 180^\circ$ +/- 7° In this case, the result of Eq. 3.3 for the proton can be applied directly (in the PWIA), after some small corrections for Fermi smearing and the deuteron D-state. The spectrum of the difference between $\phi_{electron}$ and ϕ_{proton} was used to extract the dilution due to events from ^{15}N and ^{4}He in the target material. The dilution was estimated in two different ways: 1) integrating the two side wings outside the region $\phi_e - \phi_p = 180^\circ$ +/- 10° for both ND_3 and corresponding Carbon target events and taking the ratio of the integrals as the cross-normalization between the two, and 2) double gaussian fitting of the ND_3 spectrum using constraints on the width and center extracted from the Carbon target runs. In case 1), the dilution factor was the ratio of the difference of the ND_3 counts minus the scaled Carbon target counts in the region $\phi_e - \phi_p = 180^\circ$ +/- 7°, divided by the ND_3 counts. In case 2), we used the area of the Gaussian representing the deuteron peak, divided by the sum of both Gaussians, again integrated over the same ϕ region.

The target polarization is extracted from the obtained values for $P_b P_t$ using the measured beam polarization P_b from Moller runs. The results of the two methods fairly agree within error bars, Fig [3.5], and the first two groups shows that our NMR measurements were in reasonable shape; however after run 15250 the extracted values were about half less than the NMR values. We suspect those are due to bad TE measurement or due to localized beam induced depolarization.

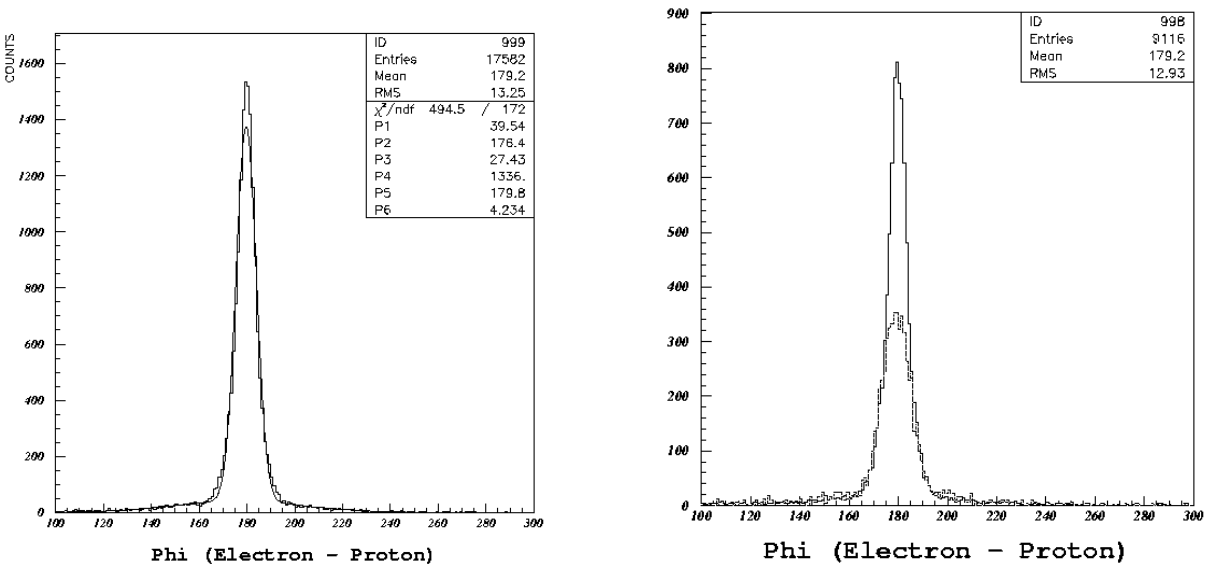

Figure 3.4: Sample of double gaussian fits (left) and the ND_3 and Carbon target spectra overlaid after the cross normalization of the "wings" (right). The dilution factor is the difference between the two spectra on the right, divided by the ND_3 total.

group	run	pb*pt	stat error
inb. 1	15360 - 15383	0.094	0.011
inb. 2	15385 - 15388	-0.061	0.023
inb. 3	15389 - 15405	0.082	0.014
inb. 4	15214 - 15235	-0.173	0.014
inb. 5	15272 - 15339	-0.080	0.017
outb. 1	15406 - 15421	0.103	0.021
outb. 2	14629 - 14679	-0.177	0.037

Table 3.5: The product of the target and beam polarization.

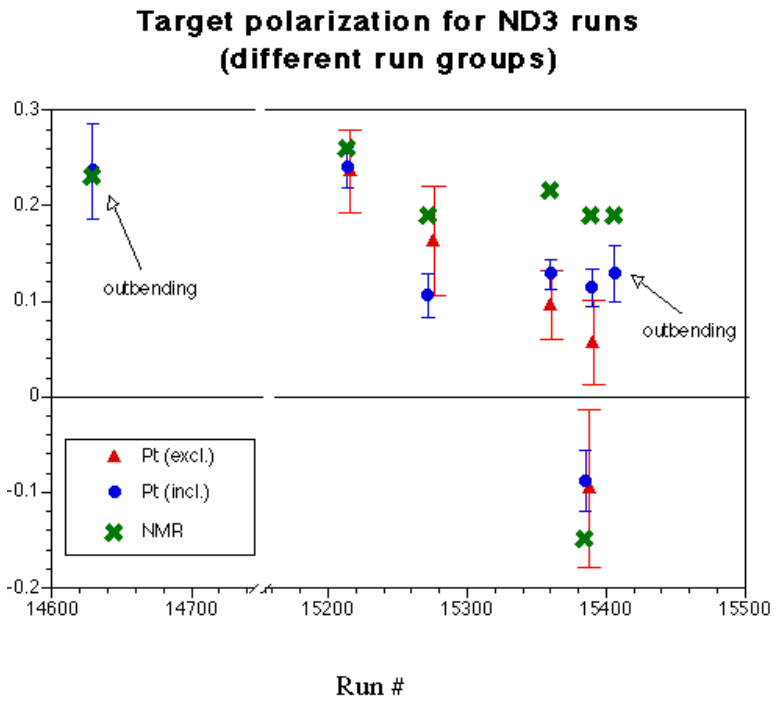

Figure 3.5: Target Polarization vs run numbers.

3.5 Dilution Factor

Since we used ND_3 as the target material, we have to deal with the contribution of non-deuteronic materials in the target like ^{15}N contained in ND_3, target windows (aluminum foils), liquid ^4He for the refrigerator etc. The fraction of the events actually scattered from the deuteron to those from *all* target materials is the dilution factor, $DF = N_{D_3}/N_{\text{full target}}$. The ^{12}C in the Carbon target was used as an approximation of the ^{15}N in the Ammonia target and

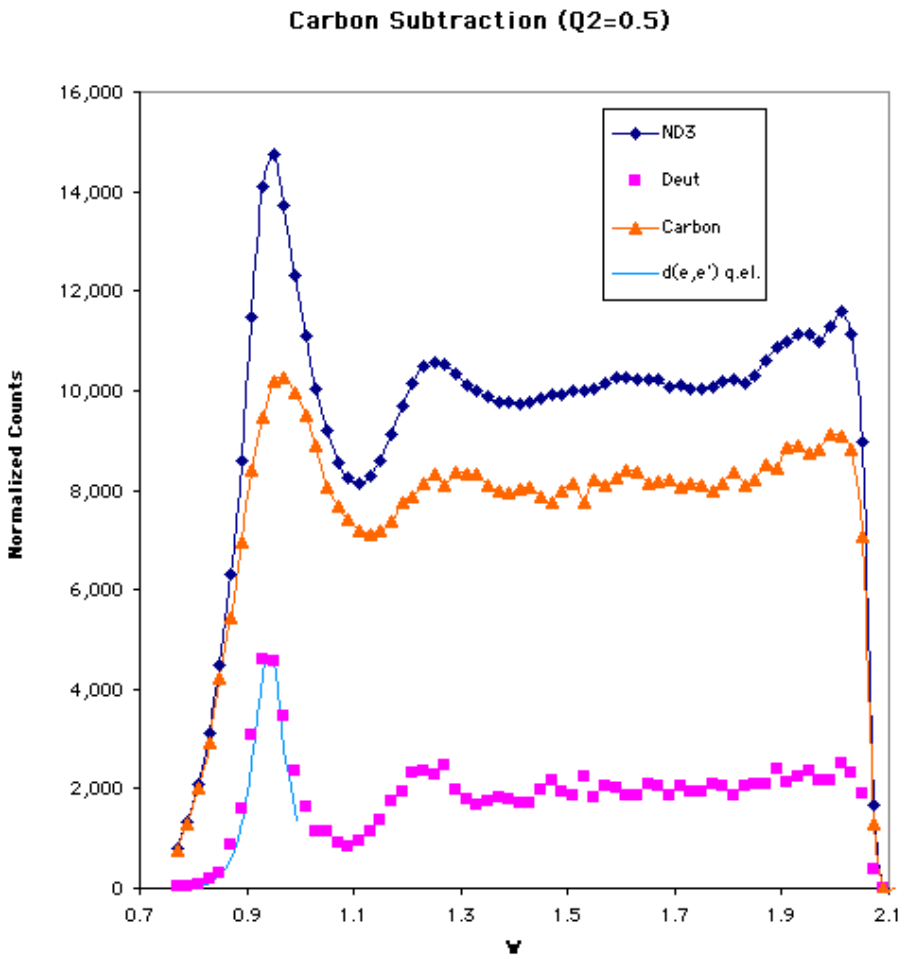

Figure 3.6: Subtraction of Carbon target data from ND_3. The top line is the measured ND_3 spectrum and the middle is the normalized Carbon target spectrum. The bottom line is the subtracted spectrum which represents the deuteron spectrum. The quasi-elastic peak is overlayed with a model calculation normalized to the data.

the dilution factor can be written as:

$$DF \approx \frac{(N_{^{15}ND_3} + N_{^4He} + N_{foils}) - A \cdot (N_{^{12}C} + N_{^4He} + N_{foils})}{(N_{^{15}ND_3} + N_{^4He} + N_{foils})} \tag{3.5}$$

The Carbon and ND_3 target runs have different statistics, and the equivalent target thicknesses (in nucleons per cm^2) as well as the effective cross sections (due to different proton/neutron ratios) are slightly different for the Carbon target versus the non-deuteronic part of the ND_3 targets. Therefore, the dilution factor estimation relies on the extraction of the ratio A of events coming from the Carbon target versus those coming from the non-deuteronic part of the ND_3 target for normalization. Eq. [3.5] can be written again as:

$$DF \approx \frac{N_{ND_3} - A \cdot N_{^{12}C}}{N_{ND_3}} \tag{3.6}$$

We have two slightly different beam energy settings, 2.494 GeV and 2.565 GeV and unfortunately only 2.565 GeV Carbon data were taken during the EG1 run period. The Carbon subtraction is not reliable for the 2.494 GeV run groups due to the detector acceptance changes between two different beam energy runs. Therefore, the dilution factor was determined by averaging within a given kinematic bin over all 2.565 GeV run groups. The same dilution factor was then applied to all run groups. This was possible since all inbending run groups were taken with the same frozen ammonia sample in the ND_3 target cell. The ratio A was extracted by comparing the quasi-elastic tails, the tail left to the quasi-elastic peak, of the Carbon and ND_3 spectra, integrated up to the W limits given in Table 3.6. The W limits were chosen such that according to model calculations only quasi-elastic scattering from ^{15}N and ^{12}C would contribute, not quasi-elastic scattering from d. These model calculations were checked by comparing the results for different W limits.

Q^2 bin	upper W limit
0.3	0.835
0.36	0.832
0.42	0.816
0.5	0.790
0.6	0.760
0.71	0.717
0.84	0.655
1.0	0.609
1.19	0.506

Table 3.6: W limits for each Q^2 bin below which the deuteron does not contribute significantly.

3.6 Polarized Nitrogen and Residual Proton Corrections

The contribution from the polarizable target nuclei in the target aside from the deuteron changes the observed asymmetries and has to be corrected for. For the target materials NH_3 and ND_3, the unpaired proton in ^{15}N and the $\approx 2\%$ of ^{14}N contamination are polarizable. The ND_3 target also needs additional corrections since it contains $\approx$1.5 % of unsubstituted or residual polarizable protons from NH_3 or ND_2H. The correction to the asymmetry may be written as [36]:

$$A_{||} = C_1 \left(A_{||}^{Raw} - C_2 \right) + A_{rc} \tag{3.7}$$

where the A_{rc} is the radiative correction. The correction factors C_1 and C_2 are given by

$$C_1^d = \frac{1}{1 - \eta_p + D_n / \left(1 - 1.5\omega_D\right)} \approx 1.02 \tag{3.8}$$

$$C_2^d = \frac{U_p F_2^p}{U_d F_2^d} \left(D_n - D_p\right) \left(A^p - A_{rc}\right) \approx -0.03 \left(A^p - A_{rc}\right) \tag{3.9}$$

with related factors
$\eta_p = \frac{\text{number of protons}}{\text{number of deuterons + number of protons}} \approx 0.015$
$\eta_N = \frac{\text{number of } ^{14}N}{\text{number of } ^{14}N + \text{number of } ^{15}N} \approx 0.02$
$D_n = \eta_N \frac{P_N}{P_d} \frac{g_{EMC}(x)}{9}$
P_N = polarization of $^{15}N = -0.40 P_d$
P_d = polarization of deuteron
$g_{EMC}(x)$ = correction for the EMC effects
$D_p = \eta_N \frac{P_p^{res}}{P_d + (2\eta_N - 1)\frac{P_N}{P_d}\frac{g_{EMC}(x)}{9}}$
P_p^{res} = residual proton polarization = 0.191+ 0.683 P_d
$1.5\omega_D$ = deuteron D-state contribution, $\omega_D \approx 0.05$
U_p, U_d = radiative corrections due to the unpolarized cross sections

Our data are not corrected for these effects, but they are included in the systematic error. Typically, C_1 is considered as a correction to the dilution factor. C_2 has a significant kinematic dependence and this correction amounted to approximately 5% of the asymmetry [44].

3.7 π^- and electron-positron pair contamination

Cerenkov counter (CC) and electromagnetic calorimeter (EC) information is used in the electron identification. The electron selectivity and pion rejection strongly depend on the π/e ratio at a given angle and momentum. The ratio of pions misidentified as electrons to the number of electrons at the same angle and momentum is a few percent with proper detector threshold and electron cuts. Our electron cut required more than 0.5 photoelectrons and $E/p > 0.2$. Matching π^- and electron E/p spectra at $E/p < 0.15$, where π^- are peaked, one can estimate the ratio of a π^- tail leaking under the electron E/p peak [Fig.3.7]. The ratio was estimated by integrating the number of π^- and electrons with $E/p > 0.2$.

In all cases, the deduced pion contamination was rather small

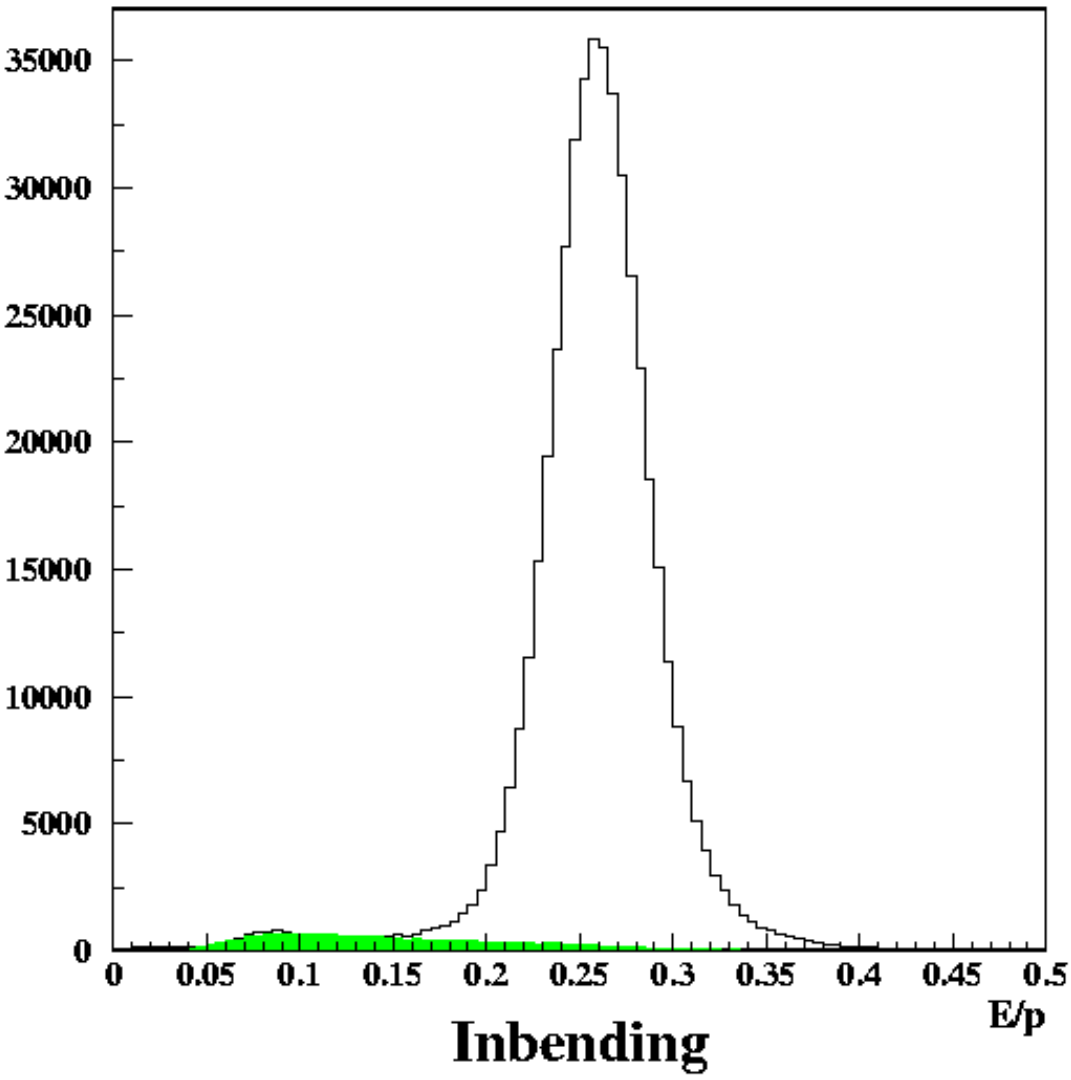

Figure 3.7: The solid line is the E/p spectrum for electrons in the EC, and the shaded histogram represents the corresponding π^- spectrum, scaled to match the electron spectrum at low E/p.

		Inbending	outbending
$0.5 < p < 0.8$	$\theta < 25^\circ$	n/a	0.5%
$0.5 < p < 0.8$	$\theta > 25^\circ$	0.87%	2.6%
$0.8 < p < 1.5$	$\theta < 25^\circ$	0.82%	1.17%
$0.8 < p < 1.5$	$\theta > 25^\circ$	0.46%	1.0%
$1.5 < p < 2.5$	$\theta < 25^\circ$	n/a	n/a
$1.5 < p < 2.5$	$\theta > 25^\circ$	n/a	n/a

Table 3.7: The ratio of π/e for each momentum and angle bin.

(below 1.2%). Since the physics source (and kinematical dependence) of this background is very similar to that from electron-positron pairs (see below) and the latter gave a larger contribution, we included the pion contamination in the treatment of this background and its systematic error. Even a much larger pion contamination would be negligible compared to the overall systematic error on the dilution factor from all sources (up to 30%).

The second source of electron contamination is electron-positron pair production primarily created from bremsstrahlung photons and the decay of a π^0. Pair-produced electrons are not distinguishable from the electron actually originating in the beam. The pair production from bremsstrahlung photons at forward angles is negligible for EG1 (since $\theta_e > 6^\circ$). The main background is e^+e^- pairs from the 1.2% decay probability of $\pi^0 \rightarrow e^+e^-\gamma$ as well as $\pi^0 \rightarrow \gamma\gamma$ followed by e^+e^- conversion of one of the two photons. The ratio of e^+/e^- can be obtained by reversing the torus polarity and comparing the combination of e^- inbending and e^+ inbending. A detailed study [41] by Peter Bosted for our experiment gave the results shown in Fig.3.8.

The correction to $A_{||}$ is given by

$$A_{||}^{corr} = A_{||}^{raw} \left(1 - rR_A\right) / \left(1 - r\right) \tag{3.10}$$

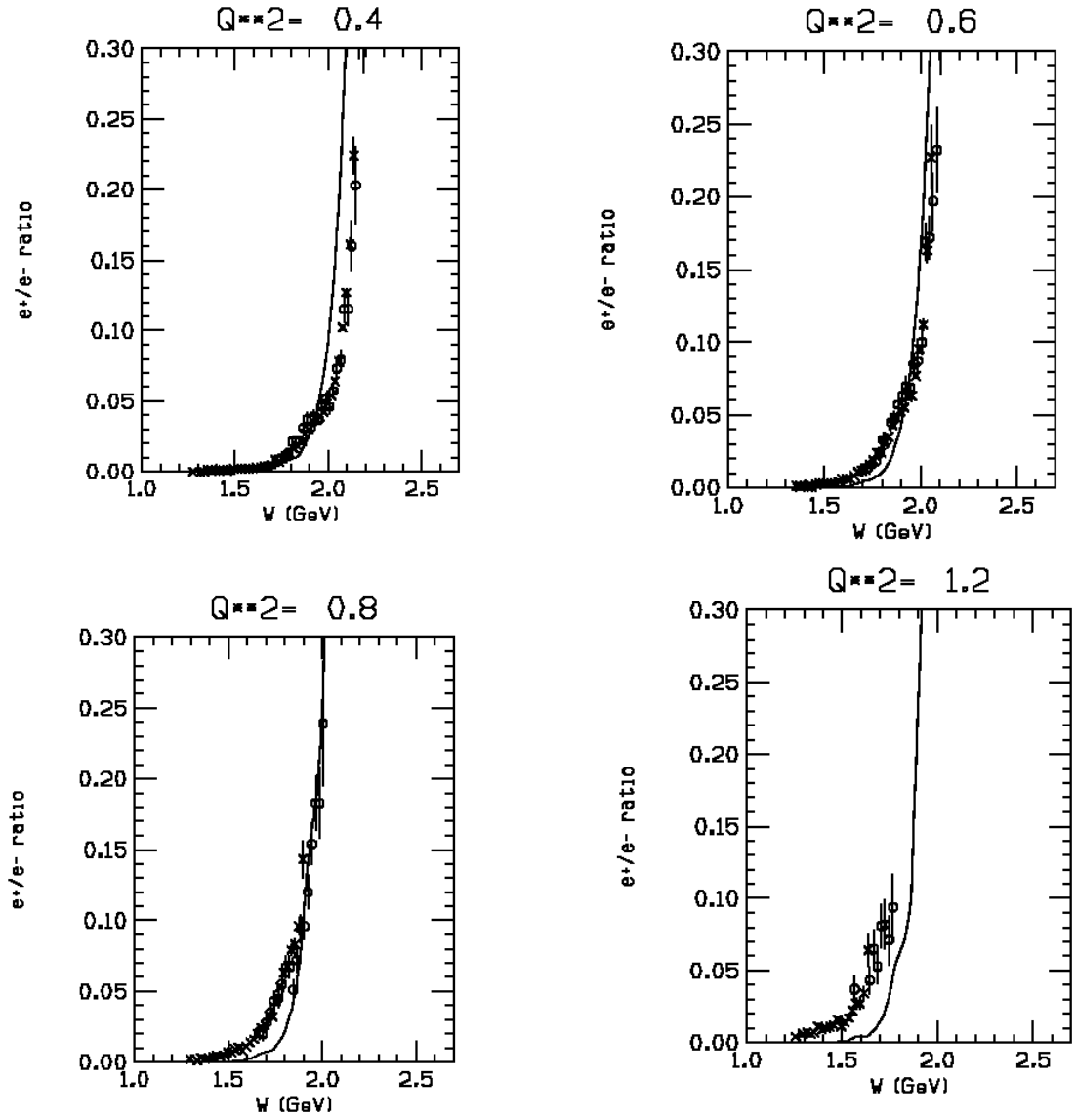

Figure 3.8: The ratio of e^+/e^- vs W. Crosses are inbending and circles are outbending data. Lines are from parametrizations following the Wiser fit. For details, see Peter Bosted's technical note.

where r is the measured e^+/e^- rate ratio and R_A is the ratio of the asymmetries for the e^+ and e^-, $R_A = A_{||}^{pos}/A_{||}^{neg}$. For our analysis, we assumed $R_A = 0$ which means that on average the asymmetry for all processes leading to e^+e^- final states is zero. Therefore, an additional dilution factor of $(1 - r)$ was applied to our asymmetries, which we took from the table generated by Peter Bosted. We used his results for a Cerenkov threshold of 0.5 photoelectrons, in agreement with our electron cut. While this threshold likely leads to an overestimation of the true dilution through electron-positron pairs, it reflects at the same time the possible size of pion contaminations to the positron (and, to some extent, electron) samples and therefore can serve as a safe upper limit for the remaining pion dilution discussed above. According to the table, the ratio r is usually less than a few percent but can rise up to 10% (lowest Q^2 bin) or even 20% (highest Q^2 bin) right at the high W edge of our kinematic range.

The assumption $R_A = 0$ is consistent with the results of Peter Bosted's analysis [41], although a slightly negative ratio $R_A < 0$ is favored. We included a systematic error corresponding to the maximum possible deviation from our assumption, $R_A = \pm 1$, in our final results.

3.8 Dead time correction

In addition to the slightly different beam charge for the two helicity states, we also have to consider the possibility of slightly different data acquisition dead times for the two helicity states. Unfortunately, during the 1998 run of EG1, we did not have dead-time gated scalers for each helicity state individually. Instead, the dead time was estimated in a two-step process. First, we used the life-time gated clock scaler to determine a linear relationship between the total data acquisition rate $\dot{n}_{DAQ}$ (typically around 1500 Hz) and the total life time fraction (ratio between the gated and the

ungated clock scaler). We found that all 2.5 GeV runs could be described reasonably well with the relationship

$$LT = 1 - 3.5 \times 10^{-5} \times \dot{n}_{DAQ} \tag{3.11}$$

resulting in an average life time of 0.95. In the second step, we used the *average* count rate for the two helicity states for each run group to calculate the helicity-dependent lifetime. Due mostly to the charge asymmetry of the electron beam, the count rate for positive helicity was about 0.3% higher than that for negative helicity (we also included the additional effect of a small rate difference due to the actual polarization-dependent scattering process). This lead to a life-time asymmetry of typically 1.6×10^{-4}, a small but not negligible correction which we applied to the integrated Faraday-cup counts for each helicity state.

3.9 Raw Asymmetry

All W spectra for ND_3 (helicty + and -) and ^{12}C were written into ASCII files for each Q^2 and W bin and each run group. We used 125 bins in W of width 0.02 GeV each, from 0 to 2.5 GeV, and 9 bins in Q^2 of width $\pm 9.4\%$ each, beginning at $0.3 \pm .028$ GeV/c^2 up to $1.2 \pm .11$ GeV/c^2. We used the inbending run groups 1, 3, 4 and 5 for the final analysis (see section 3.2). The raw asymmetries were calculated for each kinematic bin. and the Physics quantities of interest extracted separately for each group, The final results were then combined (according to their statistical weights) at the last stage. All statistical errors and group-specific systematic errors (due to beam charge asymmetries and beam and target polarization as well as dead time) were calculated for each group individually and then propogated through to the final results. Systematic errors common to all groups (dilution factor, pion contamination, radiative corrections etc.) were calculated by varying the data from each group simultaneously and recording the combined effect in the final results.

The first step was to extract the raw deuteron asymmetry $A_{||}^{raw}$ from the diluted count rate asymmetry using

$$A_{||}^{raw} = \frac{1}{DF \cdot P_b P_t} A_{||}^{dil} \tag{3.12}$$

where the diluted asymmetry is

$$A_{||}^{dil} = \frac{N^+/FC^+ - N^-/FC^-}{N^+/FC^+ - N^-/FC^-}. \tag{3.13}$$

Here N^+ and N^- are the counts from the ND_3 target for each helicity state, while FC^+ and FC^- are the life-time corrected total numbers of Faraday cup clicks for each helicity state (proportional to the integrated beam charge).

3.10 Radiative Correction

The electron travels in the bulk of target materials and may lose energy before or after the scattering off the target nucleon. These radiative energy losses are due to bremsstrahlung or ionization in external material like entrance and exit windows. The actual scattering kinematics can be changed due to the energy loss in materials along the electron's path. The corrections for these energy losses are refered as *external* radiative corrections. In addition, one has to consider the *internal* radiative corrections since the electron scattering includes contributions from higher order process as well as the Born process, a single virtual photon exchange. The longitudinal asymmetry can be written in terms of the unpolarized ($\sigma_{||}^u$) and polarized($\sigma_{||}^p$) cross sections.

$$A_{||} = \frac{\sigma^{\uparrow\downarrow} - \sigma^{\uparrow\uparrow}}{\sigma^{\uparrow\downarrow} + \sigma^{\uparrow\uparrow}} = \frac{\sigma^p}{\sigma^u} \tag{3.14}$$

The calculation of the internally radiated cross sections is decomposed into elastic, quasi-elastic and inelastic tail terms.

$$\sigma_r^p = \sigma_{Born}^p (1 + \delta_\nu) + \sigma_{el}^p + \sigma_{quasi}^p + \sigma_{inel}^p \tag{3.15}$$

$$\sigma_r^u = \sigma_{Born}^u (1 + \delta_\nu) + \sigma_{el}^u + \sigma_{quasi}^u + \sigma_{inel}^u \tag{3.16}$$

where σ_{el}, σ_{quasi} are σ_{inel} the radiative tails due to the internal bremsstrahlung for elastic, quasi-elastic and inelastic scattering processes and

$$\delta_\nu = \delta_{vert} + \delta_{vac}^l + \delta_{vac}^h \tag{3.17}$$

where δ_{vert} are the electron vertex corrections, and the δ_{vac}^l and δ_{vac}^h are the vaccum polarization correction of the lepton and the hadron respectively. We used a program which is based on the SLAC radiative correction code, RCSLACPOL by Linda Stuart. This code uses models of all Physics quantities (unpolarized and polarized structure functions) in the DIS and resonance region to calculate both unradiated (Born) and radiated (raw) asymmetries, based on the approaches developed by Kuchto and Shumeiko [42] for the internal corrections and by Tsai [43] for the external corrections, including the radiative depolarization of the beam due to the external bremsstrahlung [44]. The models used are described in the next section.

The code provides us with two numbers for each kinematic bin: The so-called radiative dilution factor

$$F_{RC} = \frac{\sigma_{Born}^u (1 + \delta_\nu) + \sigma_{inel}^u}{\sigma_{Born}^u (1 + \delta_\nu) + \sigma_{el}^u + \sigma_{quasi}^u + \sigma_{inel}^u} \tag{3.18}$$

which accounts for the fraction of the measured rate that comes from the radiated elastic and quasi-elastic tails, and the additive correction

$$A_{RC} = A_{model}^{Born} - \frac{A_{model}^{radiated}}{F_{RC}} \tag{3.19}$$

The Born asymmetry and the errors can then be written

$$A_{||}^{Born} = \frac{A_{||}^{Raw}}{F_{RC}} + A_{RC} \tag{3.20}$$

and

$$\sigma_{A_{||}}^{Born} = \frac{\sigma_{A_{||}}^{Raw}}{F_{RC}} \tag{3.21}$$

The statistical (and *systematic*) error bars of the extracted Born asymmetries are thus increased over that of the measured raw asymmetries due to the fact that the latter are "diluted" by the radiated elastic and quasielastic tails.

3.11 Model Input

Models for polarized and unpolarized structure functions are used both for radiative corrections (see previous section) and to extract Physics quantities of interest (A_1, g_1 etc.) from the measured asymmetries. All models used are based on parametrizations of world data collected by Linda Stuart, Thia Keppel, Keith Griffioen, Frank Wesselmann and the authors of the present note [47]. These parametrizations were modified by us to better describe the region of low Q^2 and low W [50].

For elastic and quasielastic scattering, form factor parametrizations for $G_{E,M}^{p,n}$ were used together with simple "Fermi-smearing" and "Pauli-suppression" corrections. Form factor fits from P. Bosted [51] were used, modified for the most recent results from JLab's Hall A [52] for the proton electric form factor G_E^p. Some alternative model fits were used for systematic studies.

The unpolarized structure functions F_1 and F_2 were modelled using the most recent fit by the NMC collaboration [58] in the DIS region and Thia Keppel's parametrization of resonance data for both the proton and the deuteron [53]. The ratio R was taken from the updated SLAC parametrization [55] ("R1998"). The low-Q^2 region was modeled by using smooth extrapolations to the existing photon point data [54]. Alternatively, we also used fits by Bodek [59] and Ricco [56] for F_1 and R for systematic studies. Neutron structure functions were extracted from the proton and deuteron fits by

first correcting the latter for Fermi-smearing of the resonance peaks (using the same PWIA Paris wave function model of the deuteron as for the quasi-elastic asymmetries).

The virtual photon asymmetry A_1 was modeled in the DIS region by an updated Q^2 and x – dependent fit to the world data [47] (SLAC, EMC, SMC, HERMES and preliminary proton results from EG1). In the resonance region, a combination of the extrapolated DIS fit and asymmetries from the code AO was used that yielded a good fit to the existing E143/E130 data. The fit was adjusted to optimize the description of our preliminary proton data from EG1. The overall fit was constrained to converge against the GDH sum rule value for the integral I^{GDH} at the real photon point.

For the photon asymmetry A_2 in the DIS region, we used an iterative fit of the Wandzura-Wilczek relation [49]

$$g_2(x) = -g_1(x) + \int_x^1 \frac{g_1(y)}{y} dy \tag{3.22}$$

which describes all existing deep inelastic data well [60]. In the resonance region, we used two different models. One assumes that the Wandzura-Wilczek relation approximately holds in this region, as well, augmented by a small "higher twist" term which is needed to ensure that the Burkardt-Cottingham sum rule [48] is fulfilled at all Q^2,

$$\int_0^1 g_2(x) dx = 0 \tag{3.23}$$

where the integral includes the elastic peak. As an alternative, we used the values for A_2 calculated wth MAID2000 up to $W = 1.7$, with a smooth interpolation to the DIS region beyond this point.

A detailed description of all models and assumptions and the actual code can be found at the secure EG1 web site [50].

3.12 Electroweak Asymmetry

The parity-violating effects from the interference between the electromagnetic and weak neutral current interactions is another source of unwanted asymmetries. The asymmetry from the interference between γ and Z^0 exchange is defined

$$A_{EW} = \frac{\sigma_R - \sigma_L}{\sigma_R - \sigma_L} \tag{3.24}$$

where σ_R and σ_L are the cross sections for the right-handed and left handed electron. Experiments[45] have been performed by scattering polarized electrons off deuterons in the deep inelastic region. The results are in agreement with the standard parton model and can be roughly parametrized[61] by

$$A_{EW} \approx -(1.0 \pm 0.3) \times 10^{-4} Q^2. \tag{3.25}$$

In our kinematic region of interest, this contribution would increase the raw asymmetry by about ≈ 5 % of its value for the deuteron. In the resonance region, the parity violating asymmetry is expected to be even smaller (of order 10^{-5}) and therefor negligible (approximately the same size as that in elastic scattering)[46]. The electroweak asymmetry only depends on the beam polarization so it can be suppressed by reversing the target polarization. This asymmetry is treated as a (negligible) contribution to our systematic error.

3.13 Extracted Physics Results

As stated before, we calculated the virtual photon asymmetry, $A_1(W, Q^2) + \eta A_2(W, Q^2)$, and the spin structure function $g_1(x, Q^2)$ for each kinematic bin and each run group separately, following the relationships listed in Chapter 2. We used our models (see Section 3.11) for the structure function R (needed to calculate D) and for F_1 and A_2 (needed to calculate g_1). Since the statistics collected

during the 1998 run of EG1 was too low to present the data in the narrow kinematic bins originally chosen, we combined every 4 bins in W and the two lowest, the three intermediate and the four highest Q^2 bin into a single value for $A_1(W,Q^2)+\eta A_2(W,Q^2)$ and $g_1(x,Q^2)$, properly weighing each bin by its statistical weight, *e.g.*:

$$g_{1_{average}} = \frac{\sum_i g_{1_i}/\sigma^2(g_{1_i})}{\sum_i 1/\sigma^2(g_{1_i})} \tag{3.26}$$

$$\sigma(g_{1_{average}}) = \left(\sum_i 1/\sigma^2(g_{1_i})\right)^{-1/2} \tag{3.27}$$

We also calculated the integral $\int g_1(x,Q^2)dx$ for each of our Q^2 bins, from pion threshold ($W = 1.08$ GeV) up to the edge of the resonance region ($W = 2.0$ GeV) or the upper kinematic limit reached by our data. The integral was approximated by converting the $\Delta W = 0.02$ GeV bins into the corresponding bin sizes Δx and summing over all bins, $\sum_i g_1(i)\Delta x_i$. Again, we combined the integrals for the two lowest, the next three, the next two and the two highest Q^2 bins to increase the statistical accuracy of the results.

As our next step, we combined the results from group 1 and 3 and those from group 4 and 5 pairwise. First, we ascertained that the results from the two run groups to be combined were consistent with each other. We did this by calculating the z-score, *e.g.*:

$$z = \frac{g_1(\text{Group1}) - g_1(\text{Group3})}{\sqrt{\sigma^2(g_1(\text{Group1})) + \sigma^2(g_1(\text{Group3}))}} \tag{3.28}$$

for each of the remaining larger kinematic bins and the integrals. From these z-scores, we then determined the average z-score for all W bins for a given Q^2 bin:

$$z_{average} = \frac{\sum_i z_i}{n} \tag{3.29}$$

Quantity	Q^2 [GeV^2/c^2]	average z	σ_z	$\chi^2/d.o.f.$
$A_1 + \eta A_2$	0.34	0.357	0.289	1.081
	0.53	-0.012	0.302	0.299
	0.99	0.078	0.333	0.705
	all	0.141	0.177	0.706
g_1	0.34	0.302	0.289	1.061
	0.53	0.041	0.302	0.278
	0.99	0.135	0.333	0.768
Integral	all	0.585	0.5	0.753

Table 3.8: Comparison of run groups 1 and 3.

as well as the total average z-score for all bins combined (and separately for all integral results as well). If the two datasets are consistent, the expectation value for these average z-scores would be zero and its standard deviation would be $1/\sqrt{n}$, where n is the number of bins entering the average. Both groups 1 and 3 and groups 4 and 5 yielded z-scores within 1.2 standard deviations. We also calculated the total χ^2 for the comparison between two groups, which again was less than 1.2 per degree of freedom in all cases.

After combining the result of group 1 with group 3 and of group 4 with group 5 (again using proper statistical weighting), we repeated the same procedure to combine the resulting two datasets into one. In this case, we found only marginal agreement between the two datasets; while all χ^2 values were within 1.2 per degree of freedom and the average z-score for the integrals was only 1.3 standard deviations off, there was a clear trend towards more negative asymmetries for the combined group 4+5 dataset for all 3 Q^2 bins (yielding an average z-score of - 0.4, about 2.3 standard deviations). Possible causes of this difference could be related to the fact that groups 1 and 3 were taken much later during the run than groups 4 and 5, with a slightly different beam energy (2.49 GeV vs. 2.57 GeV) and opposite beam polarization. However, no

Quantity	Q^2 [GeV^2/c^2]	average z	σ_z	$\chi^2/d.o.f.$
$A_1 + \eta A_2$	0.34	0.101	0.289	1.041
	0.53	-0.092	0.302	1.169
	0.99	0.617	0.333	1.226
	all	0.209	0.177	1.137
g_1	0.34	0.185	0.289	0.960
	0.53	-0.063	0.302	1.162
	0.99	0.547	0.333	1.226
Integral	all	0.456	0.5	0.627

Table 3.9: Comparison of run groups 4 and 5.

conclusive connection between these changes and the observed differences could be found, and a purely statistical fluctuation cannot be excluded. Therefore, we decided to combine these remaining two datasets as well using statistical weighing. In any case, for any given kinematical bin the average discrepancy was less than its statistical error.

The resulting values for all quantities of interest are given in Chapter 4. In the remaining Section, we discuss the treatment of and results for systematic errors.

3.14 Systematic Errors

The largest contributions to the systematic errors on the asymmetries and spin structure functions come from radiative corrections, uncertainties in the unpolarized structure functions F_1 and R, and from the ^{12}C normalization to the ND_3 spectra and the resulting error in the dilution factor. At higher Q^2 and W, the contamination with e^+e^- pairs and the uncertainty on the asymmetry A_2 also contribute significantly. The integrals have a sizable systematic error contribution from resolution effects.

In the following, we discuss each individual source of system-

Quantity	Q^2 [GeV^2/c^2]	average z	σ_z	$\chi^2/d.o.f.$
$A_1 + \eta A_2$	0.34	-0.424	0.289	1.725
	0.53	-0.499	0.302	1.057
	0.99	-0.279	0.333	0.795
	all	-0.409	0.177	1.234
g_1	0.34	-0.428	0.289	1.875
	0.53	-0.470	0.302	1.179
	0.99	-0.342	0.333	1.004
Integral	all	-0.670	0.5	0.506

Table 3.10: Comparison of combined run groups 1+3 with 4+5.

atic errors in turn. All systematic errors were evaluated by changing the corresponding analysis input parameters *simultaneously* for all 4 run groups and then look at the corresponding change in the final combined quantities (the virtual photon asymmetry $A_1(W,Q^2)+\eta A_2(W,Q^2)$, the spin structure function $g_1(x,Q^2)$, and the integrals $\Gamma_1(Q^2)$). We added the individual systematic errors in quadrature to obtain the overall sytematic error for each data point. The tables at the end of this Section give an overview of the relative contribution from the major systematic errors to each of our data points.

Helicity-dependent beam charge asymmetry
As noted before, there was a systematic difference of about 0.3% between the average number of electrons contained in each positive helicity "bucket" and the average number of electrons contained in each negative helicity "bucket". This effect has been corrected for by integrating the number of Faraday cup integrator "clicks" (1 click corresponded to 0.1 nC integrated charge) for each bucket and then normalizing the count rates for each helicity state by the total accumulated charge for that state.

Possible systematic errors on this procedure could come from

non-linearities of the Faraday cup electronics or "cross talk" between the helicity signal and the integrator. However, these errors should be only a few percent of the effect and can therefore be subsumed under the deadtime correction (see below) which is of similar magnitude. In addition, since we took data with two different beam energies and two opposite orientations of the electron spin at the target (relative to the source), this systematic error would be largely canceled in the combined results from all four run groups.

However, there is a small *statistical* error remaining which comes from the small number of clicks recorded for each 2-second bucket pair. Depending on when a given bucket begins, the very first click (which is counted as a full 0.1nC) can represent anywhere from 0 to 0.1nC *actual* accumulated charge since the beginning of the bucket, while at the end one can miss anywhere between 0 to 0.1nC of accumulated charge if the corresponding click falls outside the window of 1 second. Since the buckets are arranged in pairs of helicity states and their complements, there is also a correlation between the two buckets of such a pair (too little charge counted towards the first one automatically entails too much for the second one). The result is that there is a statistical error on the charge *difference* $Q_+ - Q_-$ of $0.1\text{nC}/\sqrt{2}$ for each bucket pair. This yields a statistical error on the charge asymmetry of $\sqrt{N_{pairs}/2}\ (0.1\text{nC}/Q_{tot})$ for a run with total integrated charge Q_{tot} and N_{pairs} bucket pairs (see also Ref. [62]).

This statistical error is independent for each run group, and was treated by increasing the statistical errors of the final results of each run group by a corresponding amount before they were combined. Since a change in the beam asymmetry affects both the Physics asymmetries of interest *and* the quasi-elastic asymmetry from which the polarization was obtained, we determined the proper additional statistical error by varying the beam asymmetry within this statistical error and then observing the resulting

change in the final results after going through the whole analysis chain again. For the inbending runs analyzed here, the additional statistical error was negligible in all cases (less than 10% of the count rate error).

CLAS detector resolution and momentum correction.
The finite CLAS detector resolution in angle and momentum of the scattered electron yields an uncertainty of about 20 MeV on the reconstructed W for each event. The systematic shift in the elastic peak position (see Section 3.3) was also on the order of a few MeV. Since the correction for this effect could only be done for the elastic peak itself, there is the possibility for an additional systematic shift in the inelastic region. Finally, the beam energy and torus current also had some associated uncertainties yielding a possible systematic error of a few MeV on the reconstructed W.

As a consequence, one can estimate that a certain fraction of electron events that were assigned to a given 20 MeV bin in W really "belonged" to an adjacent bin. We simulated the effect of this possible shift on the final Physics results by shifting all measured counts by one bin (+20 MeV) in W and recalculating all results. Of course, some of the observed change in these results is simply due to statistics: since a partially different data set enters the calculation for each kinematic bin, one can expect that the results change by the corresponding statistical uncertainty. In the case of the asymmetries $A_1 + \eta A_2$ and spin structure functions g_1, we had combined 4 W bins of 20 MeV into the final bins, so only the topmost of these 4 bins lost data and the bottommost bin contained new data after the shift. One can show that the corresponding expected statistical variation of the result is $\sigma/\sqrt{2}$ on average, where σ is the (ordinary) statistical error of the combined bin.

We used a χ^2-test to compare the final results after the shift

with those before it, with

$$\chi^2_{red} = \frac{1}{n} \sum_i \frac{(A_i - A'_i)^2}{\left(\sigma_i/\sqrt{2}\right)^2} \tag{3.30}$$

where n is the total number of W bins. For the lowest Q^2 bin the resulting χ^2 was around 0.85 per degree of freedom, indicating that the change was insignificant compared to statistics. For the upper two Q^2 bin, the χ^2 was up to 1.44 per degree of freedom, indicating that the variation was 20% larger on average than purely statistical fluctuation would predict. We assigned a systematic error of size 20% of the observed variation for each of the kinematic bins in this case. In all cases the resulting systematic error is small compared to both statistical and other systematic errors.

For the integrals Γ_1 we directly took the observed variation as the systematic error, since nearly all data entering the integral calculation remained the same (only the kinematical weighting factors changed due to the shift). The resulting variation of the integrals in all cases was less than one half of the total systematic error.

Beam and target polarization.
As described in Section 3.4, the product of beam and target polarization $P_b P_t$ was directly extracted from the measured quasi-elastic asymmetry in $\vec{d}(\vec{e}, e')$. The main error on this measurement was statistical (count rate limited); this statistical error was once again applied for each run group separately (since the polarization product was determined for each separately) and added to the total statistical error for all final results of that run group as described for the case of the charge asymmetry above. This additional statistical error was typically less than 20% of the count rate statistical error.

The largest systematic error on the determination of $P_b P_t$ stems from the dilution factor in the quasi-elastic region. Since this error is correlated with the corresponding one for the inelastic re-

gion, it is described in the next subsection. The remaining uncertainties on the theoretical value of the asymmetry (from the form factors, deuteron wave function and radiative corrections) are all much smaller than the statistical and dilution factor errors and were therefore ignored.

^{12}C and ND_3 normalization, dilution factor.
Since the dilution factor was calculated using the measured ^{12}C spectrum, any discrepancy between that spectrum and that of the non-deuteronic part of the ND_3 target (including their relative normalization) would yield an incorrect result. Possible differences between the two spectra come from the different ratios of neutrons to protons in ^{15}N versus ^{12}C, different target thickness and radiation length, different amount of liquid ^{4}He coolant and slightly different nuclear structure. Since the cross-normalization uses the low-energy "tail" of the quasi-elastic peak, nuclear structure differences (high-momentum components in the nuclear wave functions) and contamination from high-momentum components in deuterium can bias the result. Some estimate of the magnitude of these differences can be gotten from a recent run of the second part of EG1, which took data on both a pure ^{15}N target and on ^{12}C. Using the same cross-normalization method as in the present analysis, differences up to 3% where observed in the two W spectra.

We did a detailed study of different methods to determine the cross normalization, including different upper W thresholds and using exclusive $d(e, e'p)$ data as well as inclusive ones. We conclude that a safe upper limit for the uncertainty in the normalization constant A (see Eq. 3.6) is 5%. We increased this value to 6% in order to cover all additional effects described above as well as further dilution and contamination effects from polarized non-deuteronic target material. Note that the corresponding change in the dilution factor itself was about 25% of its value throughout most of the kinematic range ($\Delta DF = \Delta A/A \times (1 - DF)$, see Eq. 3.6, with a

typical value of $DF = 0.19$). By using a variation in A of 6% as an upper bound we clearly cover all other systematic errors that are proportional to the measured asymmetry (including beam and target polarization).

The effect of this systematic error on the final results was determined by changing the normalization factor by 6%, recalculating the dilution factor for all kinematic bins, recalculating the beam and target polarization $P_b P_t$ from the quasi-elastic asymmetry, and then propagating the results through the whole analysis, including the combination of the 4 groups into one.

Polarization contribution from N and H.
The nitrogen correction can be applied by two factors, C_1^d and C_2^d, Section[4.9]. The error on C_1^d is neglected since this value is very small and stable. The factor C_2^d contains the proton asymmetry and has a significant kinematic dependence. It can be calculated using the measured proton asymmetry and its error. The study from SLAC E155[44] estimates the systematic error of approximately 5% of the asymmetry. It is therefore safely included in the dilution factor systematic error which was assumed to be as much as 25% (see above).

Pair symmetric background and π^- contamination.
The effect from the electron-positron pair contamination is estimated using the measured ratio of e^+/e^- as a direct dilution factor to the asymmetry. The size of the systematic errors from the π^- contamination turned out to be smaller (less than 1%). As an upper limit for the combined systematic error from both sources, we compared our final results with and without the dilution factor as determined in Section 3.7.

Deadtime corrections.
We estimated the systematic error on our dead time correction (see

Section 3.8) by comparing the final results with and without that correction. This systematic error is negligible throughout the kinematic region.

Radiative corrections.
The systematic error from radiative corrections is due to the various model assumptions and calculational techniques used in the radiative code. We studied in detail how our final results changed with "reasonable" variations of the input models for the elastic nucleon form factors (dipole fit, Bosted fit, and Gary-Krumpelmann fit *vs.* standard fit), for the structure function R (fits by Bodek and by Ricco et al. *vs.* standard fit), for $A_2 = 0$ in the resonance region, and for different fits to A_1 in the resonance region. We also studied the effect of different treatments of quasi-elastic scattering (Fermi-momentum and Pauli blocking). We compared the results with and without peaking approximation, and for different interaction points within our target. For the asymmetries $A_1 + \eta A_2$ we also varied the model for F_1 (Bodek fit *vs.* standard fit) as part of the radiative correction error. For the structure function g_1 and the integrals Γ_1, there is a very strong correlation between the effect of F_1 on the radiative correction and the direct influence of F_1 on the conversion from measured asymmetries. Therefore, the systematic error due to F_1 was not included here but rather determined through a *simultaneous* variation of F_1 in the radiative code and in the conversion (see next subsection).

We added the largest observed variations in each of these categories in quadrature to obtain the final systematic error. This error is mostly dominated by the contributions from the elastic form factor variations and different models of A_1 in the resonance region.

Model-dependence of extracted quantities, F_1, R, A_2.
As discussed in Section 3.11, the extracted asymmetries $A_1 + \eta A_2$ depend on the value of the ratio R of longitudinal to transverse vir-

tual photon absorption cross sections. Our default model as well as the parametrization of Ricco et al. yielded only small values of $R \leq 0.1$ in the first and second resonance regions, while Bodek's parametrization gives rather large values of $R \approx 0.2$ throughout the full kinematic range. The resulting systematic error is one of the largest affecting the extracted asymmetries at low W.

In addition, the structure function F_1 is also needed to extract g_1 and the integral Γ_1 from our data. Again, we estimated this error by comparing the final results for the Bodek parametrization with our own, simultaneously replacing the Bodek fit for F_1 in both the conversion from $A_{||}$ to g_1 and in the radiative code (see previous subsection). The combined effect on g_1 and the integrals turned out to be rather small.

Finally, the asymmetry A_2 was also varied from our default model to the results from MAID2000 and to $A_2 = 0$ throughout the resonance region. The systematic error on g_1 and Γ_1 due to A_2 was taken as the maximum deviation from the "standard" results due to these two variations. This error was largest at higher values of W.

Summary of all systematic errors.
The following tables list all major systematic errors for each of the final kinematic bins for the extracted asymmetries, the spin structure functions and the integrals. Note that the systematic errors for the structure function g_1 and the integrals Γ_1 are *not* normalized to the number of nucleons (*i.e.* divided by two) as is customary in the literature.

W	StrucFunc	Dilution	Rad Corr	Resolution	pions/e+e-	TOTAL
1.12	0.053	0.181	0.082	0.000	0.000	0.207
1.20	0.048	0.007	0.037	0.000	0.000	0.061
1.28	0.064	0.014	0.045	0.000	0.000	0.081
1.36	0.027	0.021	0.060	0.000	0.000	0.069
1.44	0.010	0.010	0.024	0.000	0.000	0.028
1.52	0.007	0.008	0.012	0.000	0.000	0.017
1.60	0.002	0.003	0.014	0.000	0.000	0.015
1.68	0.003	0.021	0.009	0.000	0.001	0.023
1.76	0.001	0.005	0.008	0.000	0.003	0.011
1.84	0.002	0.012	0.012	0.000	0.005	0.017
1.92	0.008	0.019	0.012	0.000	0.014	0.028
2.00	0.001	0.001	0.008	0.000	0.005	0.009

Table 3.11: Contribution of different systematic error sources to the total systematic error for $A_1 + \eta A_2$ at $Q^2 = 0.34$ GeV^2/c^2.

W	StrucFunc	A2	Dilution	Rad Corr.	Resolution	pions/e+e-	TOTAL
1.12	0.049	0.004	0.067	0.006	0.000	0.000	0.084
1.20	0.056	0.004	0.008	0.009	0.000	0.000	0.058
1.28	0.052	0.010	0.014	0.009	0.000	0.000	0.065
1.36	0.010	0.011	0.015	0.009	0.000	0.000	0.043
1.44	0.018	0.010	0.012	0.009	0.000	0.000	0.029
1.52	0.003	0.010	0.010	0.009	0.000	0.000	0.020
1.60	0.018	0.015	0.002	0.009	0.000	0.000	0.025
1.68	0.014	0.014	0.032	0.009	0.000	0.002	0.039
1.76	0.005	0.016	0.008	0.009	0.000	0.004	0.021
1.84	0.002	0.016	0.017	0.009	0.000	0.007	0.030
1.92	0.032	0.015	0.031	0.009	0.000	0.024	0.056
2.00	0.011	0.015	0.003	0.009	0.000	0.009	0.024

Table 3.12: Contribution of different systematic error sources to the total systematic error for g_1 at $Q^2 = 0.34$ GeV^2/c^2.

W	StrucFunc	Dilution	Rad Corr	Resolution	pions/e+e-	TOTAL
1.12	0.050	0.027	0.182	0.010	0.000	0.191
1.20	0.062	0.027	0.032	0.032	0.000	0.081
1.28	0.041	0.022	0.034	0.019	0.000	0.061
1.36	0.002	0.020	0.057	0.009	0.000	0.062
1.44	0.005	0.010	0.018	0.006	0.000	0.022
1.52	0.011	0.013	0.017	0.008	0.001	0.025
1.60	0.005	0.017	0.017	0.001	0.002	0.024
1.68	0.001	0.011	0.008	0.005	0.003	0.015
1.76	0.000	0.001	0.009	0.005	0.002	0.011
1.84	0.001	0.002	0.011	0.001	0.007	0.013
1.92	0.001	0.000	0.011	0.006	0.002	0.013

Table 3.13: Contribution of different systematic error sources to the total systematic error for $A_1 + \eta A_2$ at $Q^2 = 0.53$ GeV^2/c^2.

W	StrucFunc	A2	Dilution	Rad Corr.	Resolution	pions/e+e-	TOTAL
1.12	0.000	0.004	0.003	0.007	0.001	0.000	0.008
1.20	0.029	0.002	0.016	0.007	0.003	0.000	0.034
1.28	0.007	0.006	0.012	0.016	0.002	0.000	0.022
1.36	0.011	0.006	0.007	0.024	0.001	0.000	0.028
1.44	0.004	0.009	0.005	0.008	0.000	0.000	0.013
1.52	0.007	0.012	0.012	0.014	0.002	0.001	0.023
1.60	0.006	0.018	0.016	0.010	0.000	0.002	0.027
1.68	0.008	0.017	0.012	0.006	0.001	0.004	0.023
1.76	0.007	0.019	0.002	0.006	0.002	0.002	0.022
1.84	0.003	0.020	0.003	0.011	0.000	0.009	0.025
1.92	0.008	0.020	0.001	0.013	0.002	0.003	0.025

Table 3.14: Contribution of different systematic error sources to the total systematic error for g_1 at $Q^2 = 0.53$ GeV^2/c^2.

W	StrucFunc	Dilution	Rad Corr	Resolution	pions/e+e-	TOTAL
1.12	0.060	0.004	0.109	0.000	0.000	0.125
1.20	0.033	0.010	0.016	0.000	0.000	0.038
1.28	0.009	0.001	0.023	0.000	0.001	0.025
1.36	0.003	0.010	0.045	0.000	0.001	0.046
1.44	0.007	0.010	0.012	0.000	0.003	0.017
1.52	0.009	0.030	0.011	0.000	0.012	0.035
1.60	0.008	0.030	0.016	0.000	0.015	0.038
1.68	0.004	0.018	0.005	0.000	0.019	0.027
1.76	0.004	0.013	0.009	0.000	0.029	0.033

Table 3.15: Contribution of different systematic error sources to the total systematic error for $A_1 + \eta A_2$ at $Q^2 = 0.99$ GeV^2/c^2.

W	StrucFunc	A2	Dilution	Rad Corr.	Resolution	pions/e+e-	TOTAL
1.12	0.002	0.001	0.004	0.002	0.005	0.000	0.007
1.20	0.004	0.002	0.003	0.003	0.001	0.000	0.006
1.28	0.003	0.002	0.001	0.005	0.001	0.000	0.007
1.36	0.003	0.005	0.002	0.010	0.004	0.000	0.013
1.44	0.004	0.007	0.003	0.004	0.002	0.001	0.010
1.52	0.008	0.010	0.016	0.004	0.001	0.007	0.022
1.60	0.007	0.014	0.016	0.006	0.001	0.009	0.025
1.68	0.006	0.015	0.011	0.003	0.002	0.015	0.025
1.76	0.005	0.018	0.010	0.004	0.003	0.025	0.033

Table 3.16: Contribution of different systematic error sources to the total systematic error for g_1 at $Q^2 = 0.99$ GeV^2/c^2.

Q^2	StrucFunc	A2	Dilution	Rad Corr.	Resolution	pions/e+e-	TOTAL
0.337	0.003	0.002	0.003	0.005	0.007	0.000	0.010
0.532	0.001	0.003	0.000	0.003	0.003	0.000	0.005
0.786	0.002	0.003	0.002	0.001	0.003	0.002	0.006
1.104	0.001	0.003	0.001	0.001	0.001	0.002	0.004

Table 3.17: Contribution of different systematic error sources to the total systematic error for the integrals $\Gamma_1(Q^2)$.

Chapter 4

Results

As described in the previous chapters, we extracted the asymmetries $A_1(W, Q^2) + \eta A_2(W, Q^2)$ and the spin structure functions $g_1(W, Q^2)$ and their integrals from our data. For the asymmetries and spin structure functions, we combined our original 48 bins in W (from 1.08 GeV to 2.04 GeV) into 12 larger bins of size $\Delta W = 0.08$ GeV, weighing each individual bin by its proper statistical weight (essentially the number of counts). We quote our results for each of these bins at the W of the bin center.

We also combined our original 9 bins in Q^2 into 3 new bins, again using proper statistical weighting. We calculated the average Q^2 of each of these 3 bins by weighting the individual Q^2 bins with their total number of counts within the W region of interest. The three bins had average Q^2 of 0.34 GeV^2/c^2 (ranging from 0.27 to 0.39 GeV^2/c^2), 0.53 GeV^2/c^2 (ranging from 0.39 to 0.65 GeV^2/c^2) and 1.0 GeV^2/c^2 (ranging from 0.65 to 1.3 GeV^2/c^2). The resulting values for the asymmetries and spin structure functions can be considered as averaged over the final W and Q^2 bins.

On the other hand, for the integrals only averages over Q^2 were performed while the smaller bins in W were directly integrated. In addition, the highest bin in Q^2 was subdivided into two smaller

W	$A_1 + \eta A_2$	Stat. Error	Syst. Error
1.12	0.309	0.530	0.207
1.20	-0.273	0.208	0.061
1.28	-0.406	0.169	0.081
1.36	-0.223	0.191	0.069
1.44	-0.124	0.161	0.028
1.52	-0.077	0.131	0.017
1.60	-0.036	0.119	0.015
1.68	0.140	0.102	0.023
1.76	0.063	0.101	0.011
1.84	0.055	0.086	0.017
1.92	-0.254	0.080	0.028
2.00	-0.084	0.072	0.009

Table 4.1: The measured virtual photon asymmetry $A_1 + \eta A_2$ for the deuteron at $Q^2 = 0.34$ GeV^2/c^2.

bins, with average Q^2 of 0.79 GeV^2/c^2 (ranging from 0.65 to 0.92 GeV^2/c^2) and 1.1 GeV^2/c^2 (ranging from 0.92 to 1.3 GeV^2/c^2). In the following, we will first present our results for $A_1(W, Q^2) + \eta A_2(W, Q^2)$ and then those for $g_1(W, Q^2)$ and the integrals.

4.1 $A_1 + \eta A_2$

The combination of photon asymmmetries $A_1 + \eta A_2$ extracted from our data for three different Q^2 bins are listed in Tables 4.1–4.3, together with their statistical and full systematic errors. We show the results for our intermediate Q^2 bin in Figure 4.1, together with previous data from SLAC and some model calculations. A comparison of the three different Q^2 bins can be found in Figure 4.2.

Since we didn't measure the asymmetry with the target polarization perpendicular to the electron beam ($A_\perp$), we cannot directly extract the asymmetry A_1 or A_2. The interference term A_2 is lim-

W	$A_1 + \eta A_2$	Stat. Error	Syst. Error
1.12	-0.327	0.267	0.191
1.20	-0.411	0.109	0.081
1.28	-0.316	0.090	0.061
1.36	-0.070	0.101	0.062
1.44	0.086	0.085	0.022
1.52	0.144	0.068	0.025
1.60	0.147	0.063	0.024
1.68	0.061	0.054	0.015
1.76	0.006	0.053	0.011
1.84	0.024	0.050	0.013
1.92	-0.045	0.047	0.013

Table 4.2: The measured virtual photon asymmetry $A_1 + \eta A_2$ for the deuteron at $Q^2 = 0.53$ GeV^2/c^2.

W	$A_1 + \eta A_2$	Stat. Error	Syst. Error
1.12	-0.529	0.223	0.125
1.20	-0.299	0.101	0.038
1.28	-0.106	0.083	0.025
1.36	-0.005	0.091	0.046
1.44	0.139	0.078	0.017
1.52	0.340	0.067	0.035
1.60	0.307	0.061	0.038
1.68	0.195	0.054	0.027
1.76	0.184	0.056	0.033

Table 4.3: The measured virtual photon asymmetry $A_1 + \eta A_2$ for the deuteron at $Q^2 = 0.99$ GeV^2/c^2.

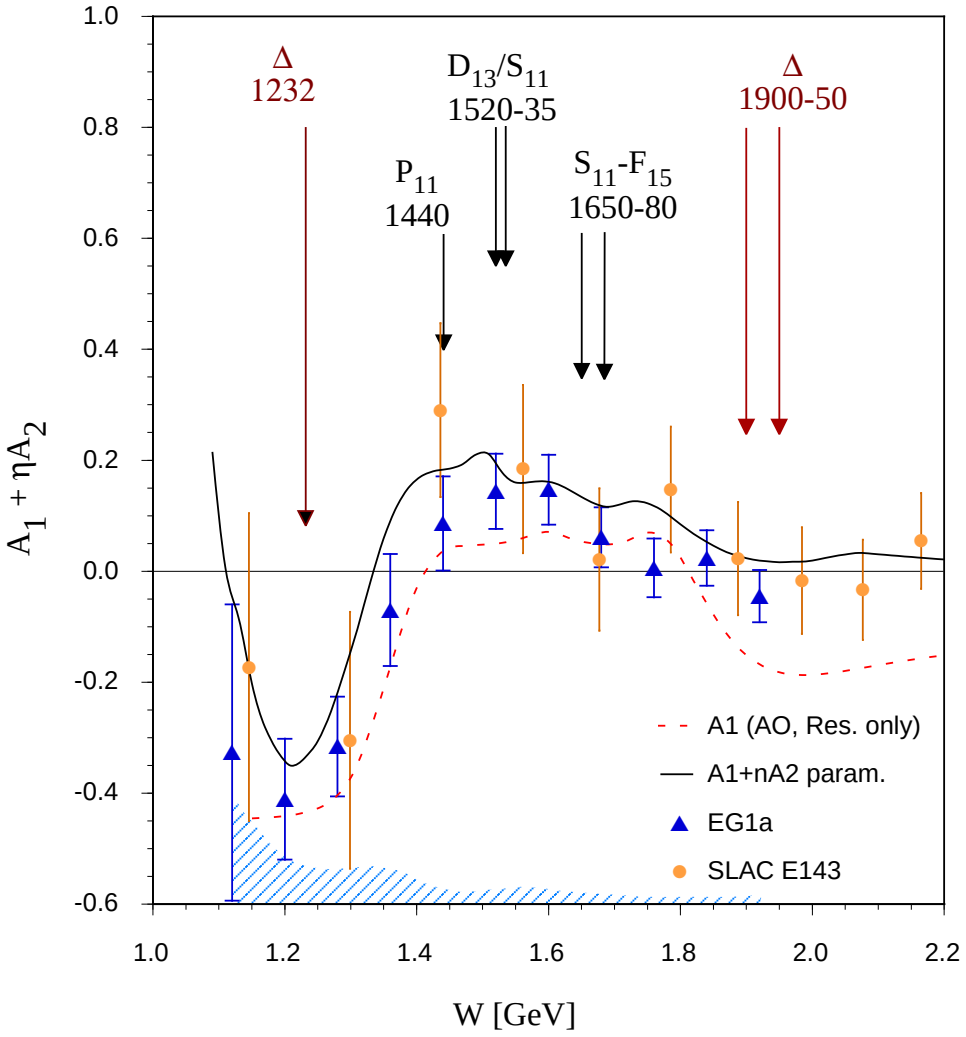

Figure 4.1: $A_1 + \eta A_2$ versus W for the $Q^2 = 0.53$ GeV^2/c^2 bin. Our data points are indicated as triangles with statistical errors only. The size of the systematic error is indicated by the shaded band at the bottom of the graph. Previous data from SLAC E143 are shown as light circles with statistical and systematic errors combined. The positions of several prominent resonances are indicated by the labeled arrows. The solid line is our model parametrization of the world data and the dashed line is the resonant contribution to A_1 from the AO parametrization.

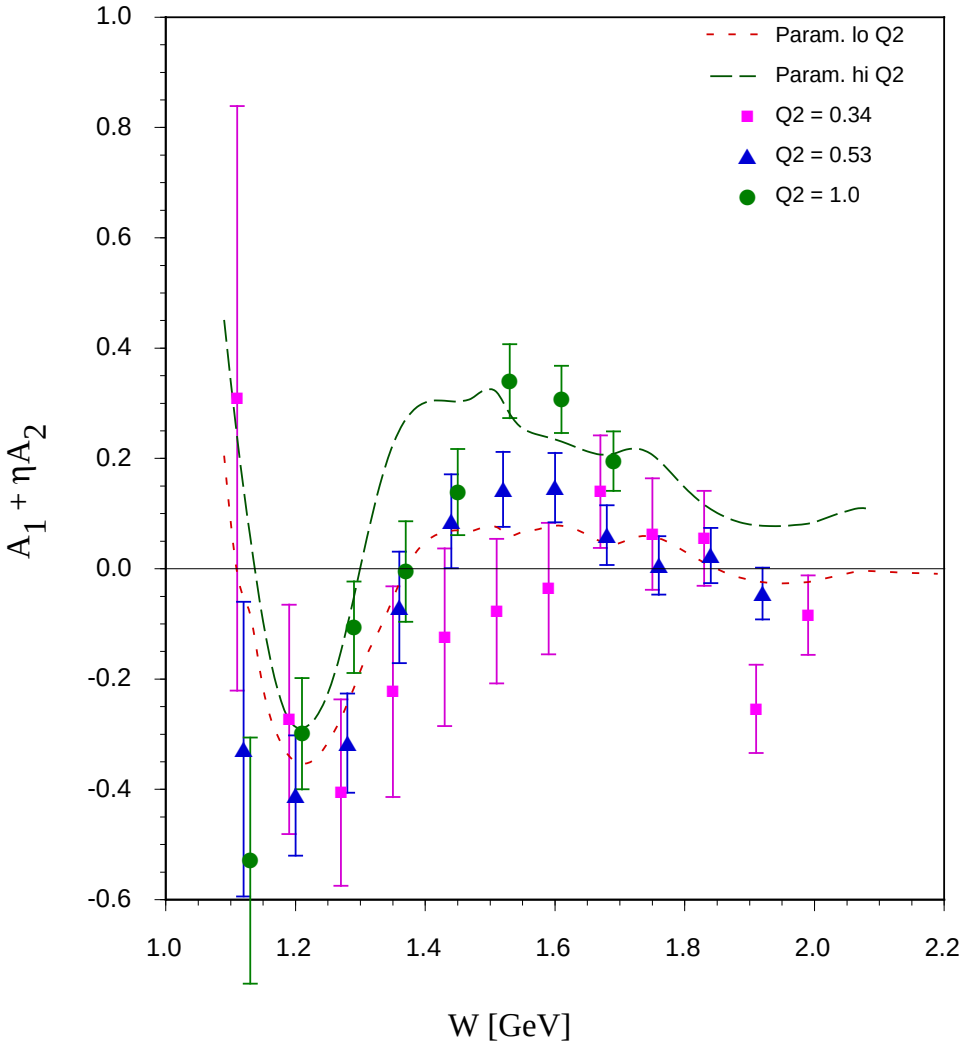

Figure 4.2: Our Data for three different bins in Q^2, together with statistical errors. (Systematic errors are highly correlated between different Q^2 bins and should have only minor effects on the observed Q^2-dependence). The long–dashed line shows our model parametrization for $Q^2 = 1.0$ GeV^2/c^2 and the short–dashed line shows our model for $Q^2 = 0.34$ GeV^2/c^2.

ited by $|A_2| < \sqrt{R}$ where the value of R is around 0.1 - 0.3 at $Q^2 = 0.5$ GeV^2 and the typical size of η for our experiment ranges from 0.1 at $W = 2$ GeV to 1.2 right at pion threshold ($W = 1.08$ GeV) at $Q^2 = 0.5$ GeV^2. Correspondingly, the asymmetry A_2 could contribute as much as 0.07 (high W) to 0.15 (at threshold) to the asymmetries shown in Figs.[4.1–4.2]. However, according to our model (see Section 3.11) this contribution should be more typically of order 0.02.

With this caveat, one can conclude that the data shown in Fig.[4.1] indeed exhibit the expected behavior for the asymmetry A_1. In the region of the Delta(1232) resonance, the asymmetry is strongly negative, and fully compatible with the naive expectation $A_1 = -0.5$. We also show the predicted full asymmetry from our model and a prediction for the resonance contribution to A_1 alone. The latter is based on the code "AO", which uses a fit of exclusive pion electro- and photoproduction data to parametrize resonant and non-resonant transition amplitudes. Beyond $W = 1.4$ GeV, the asymmetry becomes positive, indicating that $A_{1/2}$ transition amplitudes begin to dominate even at this rather low Q^2. However, even in the region of the S_{11} resonance the asymmetry is markedly smaller (around 0.15) than for the proton (around 0.4, see Ref. [63]), indicating that for the neutron alone the $A_{3/2}$ amplitude may still be larger. In general, our data agree fairly well with model predictions and the existing SLAC data, while improving significantly on the statistical errors and the resolution in W as well as the coverage down to lower Q^2 of the latter.

A comparison of our results for different Q^2, Fig.[4.2], shows a general trend to more positive asymmetries for higher Q^2, especially in the region of the S_{11} and D_{11} resonances. This is in agreement with the expected transition from $A_{3/2}$ dominance at low Q^2 (and especially at the photon point, where it yields the negative value for the GDH sum rule), and $A_{1/2}$ dominance at higher Q^2. In the limit of very large Q^2, the asymmetry A_1 in the resonance region

should become close to 1, as predicted by pQCD as well as modern quark models (Isgur) and duality arguments. A similar behavior is observed for the proton asymmetries.

Our data together with the corresponding proton results should in principle allow us to separate the different isospin contributions to the resonant and non-resonant asymmetries. However, the first run of EG1 analyzed here did not yield enough statistics to make a direct separation of proton and neutron contributions to the deuteron asymmetry feasible. In the meantime, the complete EG1 data set has been collected, which will yield a nearly tenfold improvement in statistics and a wider coverage towards both lower and higher Q^2 and higher W.

4.2 Spin Structure Function g_1 and its First Moment

The spin structure function $g_1(W, Q^2)$ was calculated from the photon asymmetry $A_1 + \eta A_2$ for each bin using

$$\begin{aligned} g_1^D(W,Q^2) &= \tfrac{\tau}{1+\tau}\left(A_1(W,Q^2) + \tfrac{1}{\sqrt{\tau}}A_2(W,Q^2)\right) F_1^D(W,Q^2) \\ &= \tfrac{\tau}{1+\tau}\left(A_1(W,Q^2) + \eta A_2(W,Q^2) + \left(\tfrac{1}{\sqrt{\tau}} - \eta\right) A_2(W,Q^2)\right) F_1^D(W,Q^2). \end{aligned} \tag{4.1}$$

Here, $F_1^D \approx F_1^p + F_1^n$ stands for the unpolarized structure function of the deuteron (not normalized). Because of the partial cancellation of the two terms in $\left(\frac{1}{\sqrt{\tau}} - \eta\right)$, g_1 is less sensitive to the asymmetry A_2 than A_1 alone. We list our results for g_1^D with their statistical and full systematic errors in Tables [4.4 - 4.6].

For the remainder of our presentation, we have divided all deuteron structure functions (F_1^D, g_1^D) by 2 to follow standard conventions (the structure functions are taken *per nucleon* in the target). In Fig. 4.3, we show our results for all three values of Q^2, plotted against the Nachtmann scaling variable $\xi = Q^2/m(\nu + q)$. This variable corresponds to Bjorken x at high Q^2 while it takes target nucleon mass corrections into account and therefore reduces

W	g_1	Stat. Error	Syst. Error
1.12	0.065	0.116	0.084
1.20	-0.230	0.160	0.058
1.28	-0.343	0.148	0.065
1.36	-0.159	0.134	0.043
1.44	-0.117	0.134	0.029
1.52	-0.079	0.155	0.020
1.60	-0.043	0.146	0.025
1.68	0.223	0.148	0.039
1.76	0.115	0.150	0.021
1.84	0.095	0.130	0.030
1.92	-0.404	0.132	0.056
2.00	-0.140	0.131	0.024

Table 4.4: The measured spin structure function g_1 for the deuteron at $Q^2 = 0.34$ GeV^2/c^2.

W	g_1	Stat. Error	Syst. Error
1.12	-0.050	0.035	0.008
1.20	-0.176	0.050	0.034
1.28	-0.166	0.047	0.022
1.36	-0.016	0.046	0.028
1.44	0.048	0.048	0.013
1.52	0.150	0.057	0.023
1.60	0.160	0.056	0.027
1.68	0.091	0.059	0.023
1.76	0.031	0.061	0.022
1.84	0.055	0.060	0.025
1.92	-0.032	0.061	0.025

Table 4.5: The measured spin structure function g_1 for the deuteron at $Q^2 = 0.53$ GeV^2/c^2.

W	g_1	Stat. Error	Syst. Error
1.12	-0.043	0.015	0.007
1.20	-0.057	0.022	0.006
1.28	-0.019	0.021	0.007
1.36	0.006	0.022	0.013
1.44	0.047	0.025	0.010
1.52	0.172	0.032	0.022
1.60	0.178	0.032	0.025
1.68	0.144	0.035	0.025
1.76	0.163	0.042	0.033

Table 4.6: The measured spin structure function g_1 for the deuteron at $Q^2 = 0.99$ GeV^2/c^2.

"*kinematical* higher twist" scaling-violating effects at lower Q^2. Together with our data, we also show as reference the prediction for $g_1(\xi, Q^2 = 10 \text{ GeV}^2)$ from our model. The assumption of local quark-hadron duality predicts that structure functions like F_1 and g_1 should, on average, approach a universal scaling curve if plotted versus the variable ξ, even in the resonance region. This is confirmed down to rather low Q^2 in the case of the unpolarized structure function F_2^p. Apparently, local duality does not work as well for the *polarized* structure function g_1 at high values of ξ where the asymmetry is dominated by the Delta resonance and therefore is negative. Overall, the approach to the "asymptotic value" for $Q^2 = 10$ GeV^2 seems to be relatively slow; only our highest Q^2 bin shows fairly good agreement beyond the region of the Delta resonance.

We integrated our results for $g_1(x, Q^2)$ over the (ordinary) Bjorken variable x for four different values of Q^2, beginning at quasi–free pion production threshold ($W = 1.08$ GeV) up to the kinematic limit of our data. We expect that these integrals are close to an incoherent average over the individual nucleons (proton and

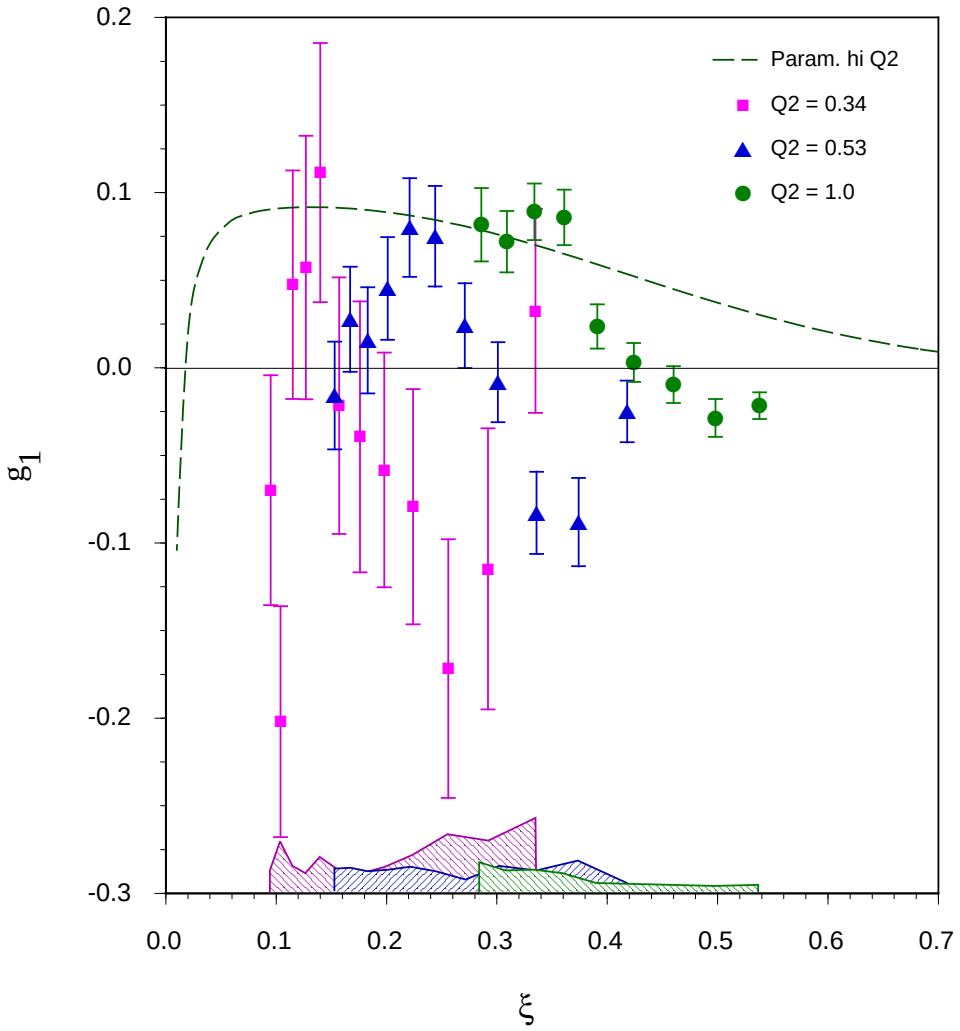

Figure 4.3: The spin structure function g_1 for the deuteron at 3 different values of Q^2, plotted against the Nachtmann variable ξ together with an extrapolation of a fit to the deep inelastic data at $Q^2 = 10$ GeV^2. Following standard conventions, all values have been divided by 2 to normalize to the number of nucleons in deuterium. The error bars are statistical only, while the shaded bands indicate systematic error bars for the three data sets.

Q^2	$W_{\max}$	Meas. Γ_1	Stat. Error	Syst. Error	Full Γ_1	Syst. Error
0.34	2.00	-0.027	0.012	0.005	-0.034	0.007
0.53	2.00	-0.008	0.004	0.002	-0.013	0.006
0.79	1.96	0.008	0.003	0.003	0.009	0.006
1.10	1.80	0.007	0.003	0.002	0.016	0.005

Table 4.7: The first moments of the spin structure function g_1 of the deuteron. Following standard convention, the integral is normalized to the number of nucleons in deuterium.

neutron) in deuterium, reduced by the D-state correction factor $(1 - 3/2P_D)$. The results are shown in the third column of Table 4.7 and the upper kinematic limits for W are listed in the second column. These upper W bounds correspond to lower limits of $x = (0.1, 0.15, 0.21, 0.32)$ for the 4 Q^2 bins, respectively. We use our model to estimate the contribution to the integral below these limits and show the resulting "full" integrals and their systematic errors in the last two columns of Table 4.7. These systematic errors include a contribution from the uncertainty of this extrapolation to $x = 0$. To estimate this uncertainty, we studied the variation of the low–x contribution due to different model assumptions; also, since there are no high-precision data below $x = 0.02$, we added a systematic error equal to the value of the integral from $x = 0$ up to 0.02.

Our results of the first moment $\Gamma_1(Q^2)$ of the spin structure function g_1 are also shown in Fig. 4.4. The solid line at higher Q^2 is a fit to the world's data extrapolated down to lower Q^2 using pQCD corrections up to second order. The dotted line indicates the slope for the integral at $Q^2 = 0$ predicted by the GDH sum rule. The dashed line (the bottom line) is the AO calculation for the contribution from the nucleon resonances only. The code AO is based on a parametrization of measured pion electro- and photoproduc-

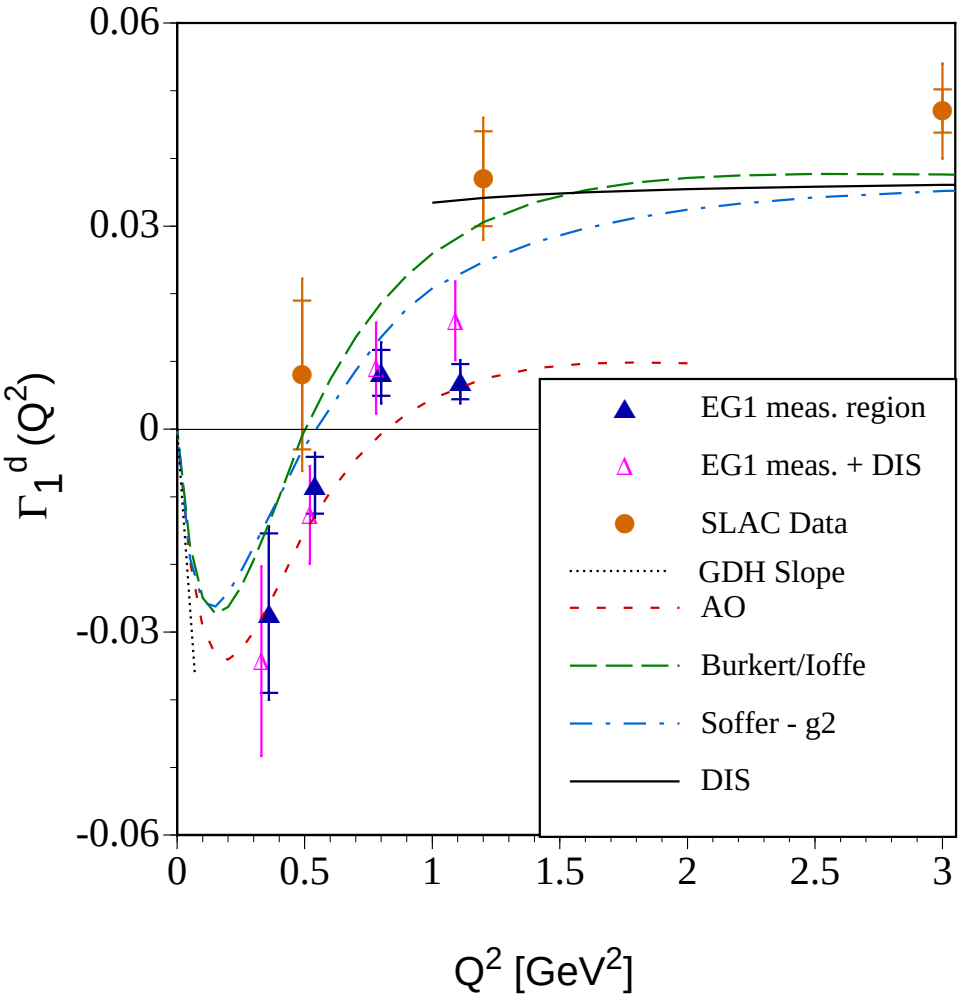

Figure 4.4: The first moment of the spin structure function g_1 of the deuteron (per nucleon). See explanations in text.

tion amplitudes. The other line labeled as Burkert/Ioffe (the top line) is the AO calculation plus a term that depends smoothly on Q^2 and interpolates between the part that is missing at $Q^2 = 0$ to saturate the GDH sum rule and the full value of Γ_1 in the high Q^2 limit. Fig. 4.4 also shows the prediction from the model by Soffer and Teryaev [29]. They use an interpolation of the integral over the structure function $g_T = g_1 + g_2$ which converges to Γ_1 at high Q^2 and remains positive down to the photon point where its slope is given by a combination of the GDH sum rule and elastic nucleon form factors. They subtract the contribution from the integral over g_2 (which is related to nucleon form factors via the Burkard-Cottingham sum rule) to obtain the integral Γ_1 alone. The solid triangles are based on EG1 data alone and the open triangles include the estimated contribution to the integral from beyond our kinematic limits. The inner error bars are statistical and the outer error bars represent the systematic errors added in quadrature. They include the uncertainty on the estimated low-x contribution for the full integrals (open triangles).

The first conclusion one can draw from Fig. 4.4 is that the integral over our measured region (essentially the resonance region) is in rather good agreement with the prediction of the AO parametrization for resonance contributions only. The data follow the predicted trend from negative values at small Q^2, where the Delta resonance contributes most of the integral and most other resonances are also dominated by the $A_{3/2}$ transition amplitude, to positive values at higher Q^2, where the $A_{1/2}$ amplitude begins to take over and the importance of the Delta is diminished. Since we did not include Born terms or other non-resonant terms in the curve labeled "AO", one can conclude that these terms must contribute relatively little to the integral over the resonance region in the case of the deuteron. This may be due to a partial cancellation between the asymmetry of the proton (which is likely positive for these terms) and that of the neutron.

Extrapolating the integral down to $x = 0$ seems to change the results only moderately (in the negative direction at low Q^2 and towards more positive values at higher Q^2). This can be understood again as a cancellation between a strongly negative-going trend of the structure function $g_1^n(x)$ as x goes to zero and a more positive trend for $g_1^p(x)$, according to existing DIS data and NLO analyses. However, this extrapolation is rather uncertain today (as it is in the DIS region), and the error bars on our open triangles may be an underestimation of that uncertainty. The evolution of our knowledge of the low–x behavior of spin structure functions over the past five years is also partially responsible for the mild discrepancy between our quoted results and those from the E143 experiment at SLAC – if we replace the published values for the full integrals with present-day extrapolations for the unmeasured region, all SLAC data points would move down by about 0.003 to 0.006. With this proviso, our data are (marginally) consistent with the SLAC data, but have much improved statistical errors and cover lower Q^2. Our data are also (marginally) consistent with both predictions for the full integral shown in Fig. 4.4, although they lie consistently below both curves (and in particular that by Burkert and Ioffe). Correspondingly, they seem to indicate a slower transition from the negative values near the photon point to the positive asymptotic value at high Q^2. The zero–crossing appears to occur somewhere between $Q^2 = 0.5$ GeV^2 and $Q^2 = 0.8$ GeV^2, significantly later than in the case of the proton.

Clearly, neither the kinematic reach (in W and Q^2) nor the statistical precision of the present data set allow a definite statement about the validity of (or the approach towards) the GDH sum rule limit. The vastly larger data set of the recently completed second run of EG1 will help dramatically in this respect. However, our data confirm the general trend required of any theory that aims to describe the spin structure of the nucleon over the full range of length scales, from the real photon point to the scaling limit.

1. Z.P. Li, V. Burkert and Zh. Li, *Phys. Rev.* **D 46** 70(1992)
2. G.P. Ramsey, *hep-ph/9702227*
3. N. Isgur, Phys. Rev. D **59**, 034013 (1999).
4. J. Ellis and R.L. Jaffe, Phys. Rev. D **9**, 1444 (1974).
5. J.D. Bjorken, Phys. Rev. **148**, 1467 (1966).
6. S.A. Larin and J.A.M. Vermaseren, *Phys. Lett.* **B 259** 345 (1991)
7. Yu. Dokshitzer, *Sov. Phys. JTEP* **46** 641 (1977)
8. V.N. Gribov and L.N. Lipatov, *Sov. J. Nucl. Phys.***15** 438 (1972)
9. G. Altarelli and G. Parisi, *Nucl. Phys.* **B 126** 298 (1977).
10. I.I. Balitsky, V.M. Braun and A.V. Kolenichenko, *Phys. Lett.* **B 242** 245-250 (1990)
11. E143, K. Abe *et al, Phys. Lett.* B **364**, 61 (1995)
12. E.D. Bloom and F.J. Gilman,Phys. Rev. Lett. **25**, 1140 (1970).
13. C.E. Carlson and N. Mukhopadhyay, Phys. Rev. D **58**, 094029 (1998).
14. S. Simula, M. Osipenko, G. Ricco and M. Taiuti, Phys. Rev. D **65**, 034017 (2002)
15. B. Ehrnsperger and A. Shafer, Phys. Rev. D **52**, 2709 (1995).
16. O. Nachtmann, *Nucl. Phys.* **B 63** 237 (1973)
17. S.B. Gerasimov, *Sov. J. Nucl. Phys.* **2**, 430 (1966)
18. S.D. Drell. and A.C. Hearn, *Phys. Rev. Lett.* **16**, 908 (1966).
19. F.E. Low, *Phys. Rev.* **96**, 1428 (1954)
20. M. Gell-Mann and M.L. Goldberger, *Phys. Rev* **96**, 1433 (1954)
21. M. Gell-Mann, M. Goldberger and W. Thirring, *Phys. Rev.* **95** 1612 (1954)
22. I. Karliner, *Phys. Rev.* **D 7** 2717 (1973)
23. R. Workman and R. Arndt, *Phys. Rev.* **D 45** 1789 (1992)
24. A.M. Sandorfi, C.S. Whisnant and M. Khandaker, Phys. Rev. D **50**, R6681 (1994).

25. J. Ahrens et al., *Phys. Rev. Lett.* **84**, 5950(2000)
26. M. Anselmino, B.L. Ioffe and E. Leader *Sov. J. Nucl. Phys.* 49 (1986) 136.
27. V. Burkert and Zhu. Li, *Phys. Rev.* **D47** 46 (1993)
28. V.D. Burkert and B.L. Ioffe *Phys. Lett.* B **296** 223 (1992)
29. J. Soffer and O. Teryaev, *Phys. Rev.* D **51** 25 (1995)
30. X. Ji and J. Osborne, hep-ph/9905410
31. D. Drechsel, S.S. Kamalov, G. Klein and L. Tiator, MKPH-T-98-19
32. E143, K. Abe *et al.*, Phys. Rev. Lett. **75**, 25 (1995).
33. E154, K. Abe *et al.*, Phys. Rev. Lett. **79**, 26 (1997).
34. HERMES, K. Ackerstaff *et al.*, Phys. Lett. **B404**, 383 (1997).
35. E130, G. Baum *et al., Phys. Rev. Lett.* **45**, 2000 (1980)
36. E143 Collaboration, K.Abe et al., *Phys. Rev. Lett.* **78** 815 (1997)
37. A.W. Thomas, *hep-ph/9708484*
38. C.Ciofi degli Atti, L.P. Kaptari, S. Scopetta, A.Yu. Umnikov and K. Kazakov, *Phys. Rev.*, **C51** (1995) 52.
39. C. Ciofi degli Atti, A. Scopetta and A.Yu. Umnikov, *nucl-th/9602026*
40. H. Arenhovel, G. KreB, R. Schmidt, and P. Wilhelm, *Phys. Lett.* B **407** (1997) 1 - 7.
41. P. Bosted, EG1 technical note, http://www.jlab.org/Hall-B/secure/eg1/Bosted/positrons.ps
42. T.V. Kukhto and N.M. Shumeiko, *Nucl. Phys.* **B 219** 412 (1983)
43. Yung-Su Tsai, *Rev. Mod. Phys.* **46** 815 (1974)
44. F.R. Wesselmann, Ph.D thesis, Old Dominion Univ. (2000)
45. C.Y. Prescott et al. *Phys. Lett.* **84 B** 524 (1979)
46. L.M. Nath, K. Schilcher and M. Kretzchmar, *Phy. Rev* **D 25** 2300 (1982)
47. P.L. Anthony, et al. (E155 collaboration), Phys. Lett. **B493**,

19 (2000).
48. H. Burkhardt and W.N. Cottingham, Ann. Phys. **56**, 453 (1970).
49. S. Wandzura and F. Wilczek, Phys. Lett. **B72**, 195 (1977).
50. S. Kuhn, http://www.jlab.org/Hall-B/secure/eg1/Models/InclusiveModels.html
51. P.E. Bosted, Phys. Rev. C **51**, 409 (1995).
52. M.K. Jones *et al.*, Phys. Rev. Lett. **84**, 1398 (2000).
53. Thia Keppel, private communication
54. See the collection of the Particle Data Group, http://www-pdg.lbl.gov/
55. K. Abe, et al. (E143 collaboration), Phys. Lett. **B452**, 194 (1999).
56. G. Ricco et al, Nucl. Phys. **B555**, 306 (1999).
57. X. Ji and W. Melnitchouk, *Phys. Rev.* **D 56** R1 (1997)
58. M. Arneodo et al. *Phys. Lett.* **B 364** (1995) 107
59. A. Bodek *et al.*, Phys. Rev. D **20**, 1471 (1979).
60. The E155x collaboration, in preparation
61. P. Bosted, SLAC E158 Technical Note (April 2000)
62. M. Anghinolfi et al. , CLAS Note 2001-20.
63. R. Fatemi, Ph.D. thesis UVa and CLAS analysis note.